

Coupling BM3D with directional wavelet packets for image denoising

Amir Averbuch¹ Pekka Neittaanmäki² Valery Zheludev¹ Moshe Salhov¹ Jonathan Hauser³

¹School of Computer Science, ³School of Electrical Engineering
Tel Aviv University, Israel

²Faculty of Mathematical Information Technology
University of Jyväskylä, Finland

Abstract

The paper presents an image denoising algorithm by combining a method that is based on directional quasi-analytic wavelet packets (qWPs) with the popular BM3D algorithm. The qWPs and its corresponding transforms are designed in [1]. The denoising algorithm qWP (qWPdn) applies an adaptive localized soft thresholding to the transform coefficients using the *Bivariate Shrinkage* methodology. The combined method consists of several iterations of qWPdn and BM3D algorithms, where the output from one algorithm updates the input to the other (cross-boosting). The qWPdn and BM3D methods complement each other. The qWPdn capabilities to capture edges and fine texture patterns are coupled with utilizing the sparsity in real images and self-similarity of patches in the image that is inherent in the BM3D. The obtained results are quite competitive with the best state-of-the-art algorithms. We compare the performance of the combined methodology with the performances of cptTP-CTF₆, DAS-2 algorithms, which use directional frames and the BM3D algorithm. In the overwhelming majority of the experiments, the combined algorithm outperformed the above methods.

1 Introduction

High quality denoising is one of the main challenges in image processing. It tries to achieve suppression of noise while capturing and preserving edges and fine structures in the image. A huge number of publications related to a variety of denoising methods (see, for example the review [7]) exist. One successful method is the BM3D algorithm ([6]), which exploits the self-similarity of patches and sparsity of the image in a transform domain. This method is incomparable in restoration of moderately noised images. However, the BM3D tends to over-smooth and smears the image fine structure and edges when noise is strong. Also, the BM3D is not successful when the image contains many edges oriented in multiple directions. On the other hand, algorithms that use directional waveforms provide the opportunity to capture lines, edges and texture details. Recently, tight tensor-product complex wavelet frames (TP-CTF_n) with different number of directions, are described in [8, 9] and some of them, in particular bandlimited TP-CTF₆ and compactly supported cptTP-CTF₆ ([17]), demonstrate a remarkable performance in image denoising and inpainting.

Some disadvantages of the above 2D (cpt)TP-CTF₆ frames such as, for example, limited and fixed number of directions (14 directions at each decomposition level) are overcome by the algorithm *Digital Affine Shear Filter Transform with 2-Layer Structure* (DAS-2) by the incorporation of

the two-layer structure, which is inherent in the (cpt)TP-CTF₆, into directional shearlet-based filter banks introduced in [10, 18]. This improves the performance of the DAS-2 compared to the TP-CTF₆ on texture-rich images such as “Barbara” and, especially, “Mandrill”, which is not the case with more regular images such as “Lena”, “Boat” and “Goldhill”.

Complex wavelet frames are the extensions of complex wavelets introduced by Kingsbury [11, 12]. Another extensions are complex wavelet packets (Co-WPs). Recently, a family of Co_WP transforms is designed in [1], which are referred to as quasi-analytic WPs (qWPs). As a base for the design, the family of WPs originated from periodic discrete splines of different orders, which are described in [2] (Chapter 4), is used. The qWPs possess valuable properties such as perfect frequency separation, Hilbert transform relation between real and imaginary parts of the WPs and orthonormality of shifts of their real and imaginary parts. The two-dimensional (2D) qWPs are derived by a standard tensor products of 1D qWPs. The number of directions of the 2D qWPs depends on the decomposition level. To be specific, the WPs from level m are oriented in $2(2^{m+1}-1)$ directions. The waveforms are close to directional cosines with various frequencies modulated by localized low-frequency 2D signals. Both one- and two-dimensional transforms are implemented in a very fast ways by using FFT.

Due to the above properties, a qWP-based algorithm (qWPdn), which utilizes a version of the Bivariate Shrinkage algorithm (BSA [15, 5]), proved to be efficient for image denoising. Experiments with the qWPdn demonstrate its ability to restore edges and texture details even from severely degraded images. In most experiments, the qWPdn to be described in Section 4.1 provides better resolution of edges and fine structures compared to the cptTP-CTF₆, DAS-2 and BM3D algorithms, which is reflected in getting higher SSIM values. On the other hand, the BM3D algorithm proved to be superior in the noise suppression, especially in smooth regions of images, thus producing the highest PSNR values in almost all the experiments. However, some over-smoothing effect on the edges and fine texture persisted under the BM3D algorithm. Especially, this is the case for severely degraded images.

Therefore, it is natural to combine the qWPdn and BM3D algorithms in order to retain strong features of both algorithms and to get rid of their drawbacks. The hybrid qWPdn-BM3D algorithms presented in the paper consist of the iterated execution of the qWPdn and BM3D algorithms in a way that the output from one algorithm updates the input to the other. Typically, 2–3 (rarely 5–6) iterations are needed to get an excellent result. In multiple experiments, part of which is reported in Section 4.3, the qWPdn-BM3D algorithms demonstrate noise suppression efficiency that is quite competitive with BM3D. Thus, it produces PSNR values higher than or very close to the values BM3D produces. On the other hand, its performance related to edge resolution and fine structures was much better than the performance of BM3D, thus, producing significantly higher SSIM values. In almost all the experiments the performance of the cptTP-CTF₆ and DAS-2 algorithms were inferior to what qWPdn-BM3D algorithms produce .

The paper is organised as follows: In order the paper to be self-contained, Section 2 and 3 briefly outline the design and implementation of the qWP transforms in one and two dimensions. Section 4.1 describes the qWPdn algorithm. Section 4.2 presents the hybrid qWPdn-BM3D algorithms. In the multiple experiments in Section 4.3, the performance of these algorithms is compared with the performance of the cptTP-CTF₆, DAS-2 and BM3D algorithms. Section 5 provides a brief discussion of the results.

Notation and abbreviations: $N = 2^j$, $\omega \stackrel{\text{def}}{=} e^{2\pi i/N}$ and $\Pi[N]$ is a space of real-valued N -periodic signals. $\Pi[N, N]$ is the space of two-dimensional N -periodic arrays in both vertical and horizontal directions. The sequence $\delta[k] \in \Pi[N]$ means the N -periodic Kronecker delta.

The abbreviation PR means perfect reconstruction. HT is the Hilbert transform, $H(\mathbf{x})$ is the discrete periodic HT of a signal \mathbf{x} .

The abbreviations WP, dsWP, cWP and qWP mean wavelet packet, orthonormal discrete spline-based wavelet packet $\psi_{[m],l}^{2r}$, complimentary wavelet packet $\varphi_{[m],l}^{2r}$ and quasi-analytic wavelet packets $\Psi_{\pm[m],l}^{2r}$, respectively, in a 1D case, and wavelet packet $\psi_{[m],j,l}^{2r}$, complimentary wavelet packet $\varphi_{[m],j,l}^{2r}$ and quasi-analytic wavelet packets $\Psi_{\pm[m],l,j}^{2r}$, respectively, in a 2D case.

qWPDn designates the qWP-based image denoising algorithm. qWPDn-BM3D means the hybrid image denoising algorithm combining the qWPDn with the BM3D.

PSNR means Peak Signal-to-Noise ratio in decibels (dB). SSIM means Structural Similarity Index ([16]). BSA stands for Bivariate Shrinkage algorithm ([5, 15]) and p-filter means periodic filter.

BM3D stands for *Block-matching and 3D filtering* ([6]), cptTP-CTF stands for *Compactly Supported Tensor Product Complex Tight Framelets with Directionality* ([17]) and DAS-2 stands for *Digital Affine Shear Filter Transform with 2-Layer Structure* ([3]).

Quadrants of the 2D frequency domain are denoted by:

$$\begin{aligned} \mathbf{Q}_0 : \{k, n = 0, \dots, N/2 - 1\}, \quad \mathbf{Q}_1 : \{k = 0, \dots, N/2 - 1, n = -N/2, \dots, -1\}, \\ \mathbf{Q}_2 : \{k, n = -N/2, \dots, -1\}, \quad \mathbf{Q}_3 : \{k = -N/2, \dots, -1, n = 0, \dots, N/2 - 1\}. \end{aligned} \quad (1.1)$$

2 (Quasi-)analytic and complementary WPs

In this section and Section 4, we briefly outline the design and properties of analytic and so-called quasi-analytic WPs (qWPs). For details we refer to [1].

2.1 Orthonormal WPs originated from discrete splines

The qWPs are derived from the periodic WPs originating from orthonormal discrete splines of different orders (dsWPs), which are described in Chapter 4 in [2] (a brief outline is given in [1]). The dsWPs are denoted by $\psi_{[m],l}^{2r}$, where $2r$ means the generating discrete spline's order, m is the decomposition level and $l = 0, \dots, 2^m - 1$, is the index of an m -level wavelet packets. The 2^m -sample shifts $\bigoplus_{l=0}^{2^m-1} \bigoplus_{k=0}^{N/2^m} \psi_{[m],l}^{2r}(\cdot - 2^m k)$ of the m -level dsWPs form an orthonormal basis of the space $\Pi[N]$ of N -periodic discrete-time signals. Surely, other orthonormal bases are possible, for example, wavelet and Best bases ([4]).

The transforms with dsWPs to the first decomposition level and back are implemented in the frequency domain using the fast Fourier transform (FFT) with the analysis and synthesis unitary modulation matrices $\tilde{\mathbf{M}}[n]$ and $\mathbf{M}[n]$, respectively:

$$\tilde{\mathbf{M}}[n] = \begin{pmatrix} \frac{\cos^{2r} \frac{\pi n}{N}}{\sqrt{U[n]}} & \frac{\sin^{2r} \frac{\pi n}{N}}{\sqrt{U[n]}} \\ \omega^n \frac{\sin^{2r} \frac{\pi n}{N}}{\sqrt{U[n]}} & -\omega^n \frac{\cos^{2r} \frac{\pi n}{N}}{\sqrt{U[n]}} \end{pmatrix}, \quad \mathbf{M}[n] = \tilde{\mathbf{M}}[n]^T, \quad U[n] \stackrel{\text{def}}{=} \frac{\cos^{4r} \frac{\pi n}{N} + \sin^{4r} \frac{\pi n}{N}}{2}. \quad (2.1)$$

The transforms from m -th to $m+1$ -th level and back are executed using the modulation matrices $\tilde{\mathbf{M}}[2^m n]$ and $\mathbf{M}[2^m n]$, respectively.

The waveforms $\psi_{[m],l}^{2r}[k]$ are symmetric, well localized in the spatial domain and have oscillatory structure, their DFT spectra form a refined split of the frequency domain. Their shapes tend to rectangular as the spline's order $2r$ grows.

A common way to extend 1D WP transforms to multiple dimensions is by the tensor-product extension. The 2D dsWPs from the level m are: $\psi_{[m],j,l}^{2r}[k, n] \stackrel{\text{def}}{=} \psi_{[m],j}^{2r}[k] \psi_{[m],l}^{2r}[n]$. Their 2^m -sample shifts along vertical and horizontal directions form an orthonormal basis of the space $\Pi[N, N]$ of 2D signals N -periodic in both directions.

2.2 Analytic periodic signals

Assume that a signal $\mathbf{x} \in \Pi[N]$ is represented by its inverse DFT, which can be written as

$$x[k] = \frac{\hat{x}[0] + (-1)^k \hat{x}[N/2]}{N} + \frac{2}{N} \sum_{n=1}^{N/2-1} \frac{\hat{x}[n] \omega^{kn} + (\hat{x}[n] \omega^{kn})^*}{2}.$$

Here \cdot^* means the complex conjugation. Define the real-valued signal $\mathbf{h} \in \Pi[N]$ and two complex-valued signals $\bar{\mathbf{x}}_+$ and $\bar{\mathbf{x}}_-$ such that

$$h[k] \stackrel{\text{def}}{=} \frac{2}{N} \sum_{n=1}^{N/2-1} \frac{\hat{x}[n] \omega^{kn} - \hat{x}[n]^* \omega^{-kn}}{2i},$$

$$\bar{x}_{\pm}[k] \stackrel{\text{def}}{=} x[k] \pm ih[k] = \frac{\hat{x}[0] + (-1)^k \hat{x}[N/2]}{N} + \frac{2}{N} \sum_{n=1}^{N/2-1} \begin{cases} \hat{x}[n] \omega^{kn}, & \text{for } \bar{x}_+; \\ \hat{x}[n]^* \omega^{-kn}, & \text{for } \bar{x}_-. \end{cases}$$

The signal $\mathbf{h} = H(\mathbf{x})$ can be regarded as the Hilbert transform (HT) of a discrete-time periodic signal \mathbf{x} and the complex-valued signals $\bar{\mathbf{x}}_{\pm}$ are the analytic signals related to \mathbf{x} ([13] for example).

2.3 Analytic WPs

The analytic spline-based WPs and their DFT spectra are derived from the corresponding dsWPs $\{\psi_{[m],l}^{2r}\}$, $m = 1, \dots, M$, $l = 0, \dots, 2^m - 1$, in line with the scheme in Section 2.2. Recall that for all $l \neq 0$, the DFT $\hat{\psi}_{[m],l}^{2r}[0] = 0$ and for all $l \neq 2^m - 1$, the DFT $\hat{\psi}_{[m],l}^{2r}[N/2] = 0$.

Denote by $\theta_{[m],l}^{2r} = H(\psi_{[m],l}^{2r})$ the discrete periodic HT of the wavelet packet $\psi_{[m],l}^{2r}$. Then, the corresponding analytic WPs are $\bar{\psi}_{\pm[m],l}^{2r} = \psi_{[m],l}^{2r} \pm i\theta_{[m],l}^{2r}$.

Properties of the analytic WPs

1. The DFT spectra of the analytic WPs $\bar{\psi}_{+[m],l}^{2r}$ and $\bar{\psi}_{-[m],l}^{2r}$ are located within the bands $[0, N/2]$ and $[-N/2, 0]$, respectively.
2. The real component $\psi_{[m],l}^{2r}$ is the same for both WPs $\bar{\psi}_{\pm[m],l}^{2r}$. It is a symmetric oscillating waveform.
3. The HT WPs $\theta_{[m],l}^{2r} = H(\psi_{[m],l}^{2r})$ are antisymmetric oscillating waveforms.

4. For all $l \neq 0, 2^m - 1$, the norms $\|\theta_{[m],l}^{2r}\| = 1$ and the magnitude spectra $|\hat{\theta}_{[m],l}^{2r}[n]|$ coincide with the magnitude spectra of the respective WPs $\psi_{[m],l}^{2r}$. When either $l = 0$ or $l = 2^m - 1$, the magnitude spectra of $\theta_{[m],l}^{2r}$ coincide with that of $\psi_{[m],l}^{2r}$ everywhere except for the points $n = 0$ or $n = N/2$, respectively.
5. For all $l \neq 0, 2^m - 1$, the shifts of the HT WPs $\{\theta_{[m],l}^{2r}[\cdot - 2^m l]\}$ are orthogonal to each other in the space $\Pi[N]$. The orthogonality does not take place for $\theta_{[m],0}^{2r}$ and $\theta_{[m],2^m-1}^{2r}$.

2.4 Complementary set of wavelet packets and quasi-analytic WPs

2.4.1 Complementary orthonormal WPs

The dsWPs $\{\psi_{[m],l}^{2r}\}$ are normalized and their 2^m -sample shifts are mutually orthogonal. Combinations of shifts of several wavelet packets can form orthonormal bases for the signal space $\Pi[N]$. It is not true for the set $\{\theta_{[m],l}^{2r}\}$, $l = 0, \dots, 2^m - 1$, of antisymmetric waveforms, which are the HTs of the WPs $\{\psi_{[m],l}^{2r}\}$. At the decomposition level m , the waveforms $\{\theta_{[m],l}^{2r}\}$, $l = 1, \dots, 2^m - 2$, are normalized and their 2^m -sample shifts are mutually orthogonal, but the norms of the waveforms $\theta_{[m],0}^{2r}$ and $\theta_{[m],2^m-1}^{2r}$ are close but not equal to 1 and their shifts are not mutually orthogonal. It happens because the values $\hat{\theta}_{[m],j}^{2r}[0]$ and $\hat{\theta}_{[m],j}^{2r}[N/2]$ are missing in their DFT spectra. Keeping this in mind, we upgrade the set $\{\theta_{[m],l}^{2r}\}$, $l = 0, \dots, 2^m - 1$ in the following way.

Define a set $\{\varphi_{[m],l}^{2r}\}$, $m = 1, \dots, M$, $l = 0, \dots, 2^m - 1$, of signals from the space $\Pi[N]$

$$\varphi_{[m],l}^{2r}[k] \stackrel{\text{def}}{=} \hat{\psi}_{[m],l}^{2r}[0]/N + \hat{\psi}_{[m],l}^{2r}[N/2]/N + \theta_{[m],l}^{2r}[k]. \quad (2.2)$$

For all $l \neq 0, 2^m - 1$, the signals $\varphi_{[m],l}^{2r}$ coincide with the $\theta_{[m],l}^{2r} = H(\psi_{[m],l}^{2r})^1$.

Proposition 2.1

- The magnitude spectra $|\hat{\varphi}_{[m],l}^{2r}[n]|$ coincide with the magnitude spectra of the respective WPs $\psi_{[m],l}^{2r}$.
- For any $m = 1, \dots, M$, and $l = 1, \dots, 2^m - 2$, the signals $\varphi_{[m],l}^{2r}$ are antisymmetric oscillating waveforms. For $l = 0$ and $l = 2^m - 1$, the shapes of the signals are near antisymmetric.
- The orthonormality properties, which are similar to the properties of WPs $\psi_{[m],l}^{2r}$, hold for the signals $\varphi_{[m],l}^{2r}$ such that $\langle \varphi_{[m],l}^{2r}[\cdot - p 2^m], \varphi_{[m],\lambda}^{2r}[\cdot - s 2^m] \rangle = \delta[\lambda, l] \delta[p, s]$.

We call the signals $\{\varphi_{[m],l}^{2r}\}$, $m = 1, \dots, M$, $l = 0, \dots, 2^m - 1$, the *complementary wavelet packets* (cWPs). Similarly to the WPs $\{\psi_{[m],l}^{2r}\}$, combinations of the cWPs can provide a variety of orthonormal bases for the space $\Pi[N]$.

¹Recall that the values $\hat{\psi}_{[m],l}^{2r}[0]/N$ and $\hat{\psi}_{[m],l}^{2r}[N/2]/N$ are real.

2.4.2 Quasi-analytic WPs

The sets of complex-valued WPs, which we refer to as the quasi-analytic wavelet packets (qWP), are defined as $\Psi_{\pm[m],l}^{2r} = \psi_{[m],l}^{2r} \pm i\varphi_{[m],l}^{2r}$, $m = 1, \dots, M$, $l = 0, \dots, 2^m - 1$, where $\varphi_{[m],l}^{2r}$ are the cWPs defined in Eq. (2.2). The qWPs $\Psi_{\pm[m],l}^{2r}$ differ from the analytic WPs $\bar{\psi}_{\pm[m],l}^{2r}$ by adding two values $\pm i\hat{\psi}_{[m],l}^{2r}[0]$ and $\pm i\hat{\psi}_{[m],l}^{2r}[N/2]$ into their DFT spectra, respectively. For a given decomposition level m , these values are zero for all l except for $l_0 = 0$ and $l_m = 2^m - 1$. It means that for all l except for l_0 and l_m , the qWPs $\Psi_{\pm[m],l}^{2r}$ are analytic. The DFTs of qWPs are

$$\hat{\Psi}_{+[m],l}^{2r}[n] = \begin{cases} (1+i)\hat{\psi}_{[m],l}^{2r}[n], & \text{if } n = 0, N/2; \\ 2\hat{\psi}_{[m],l}^{2r}[n], & \text{if } 0 < n < N/2; \\ 0 & \text{if } -N/2 < n < 0, \end{cases} \quad \hat{\Psi}_{-[m],l}^{2r}[n] = \begin{cases} (1-i)\hat{\psi}_{[m],l}^{2r}[n], & \text{if } n = 0, N/2; \\ 0 & \text{if } 0 < n < N/2; \\ 2\hat{\psi}_{[m],l}^{2r}[n], & \text{if } -N/2 < n < 0. \end{cases} \quad (2.3)$$

Figure 2.1 displays the dsWPs $\psi_{[3],l}^6 = \Re(\Psi_{\pm[3],l}^6)$ and cWPs $\varphi_{[3],l}^6 = \Im(\Psi_{\pm[3],l}^6)$, $l = 0, \dots, 7$ from the third decomposition level, and their magnitude spectra that coincide with each other. These WPs provide a collection of diverse symmetric and antisymmetric well localized waveforms, which range from smooth wavelets for $l = 0, 1$ to fast oscillating transients for $l = 5, 6, 7$. Thus, this collection is well suited to catching smooth as well as oscillating patterns in signals. In the 2D case to be discussed in Section 3, these valuable properties of the spline-based wavelet packets are completed by the directionality of the tensor-product waveforms.

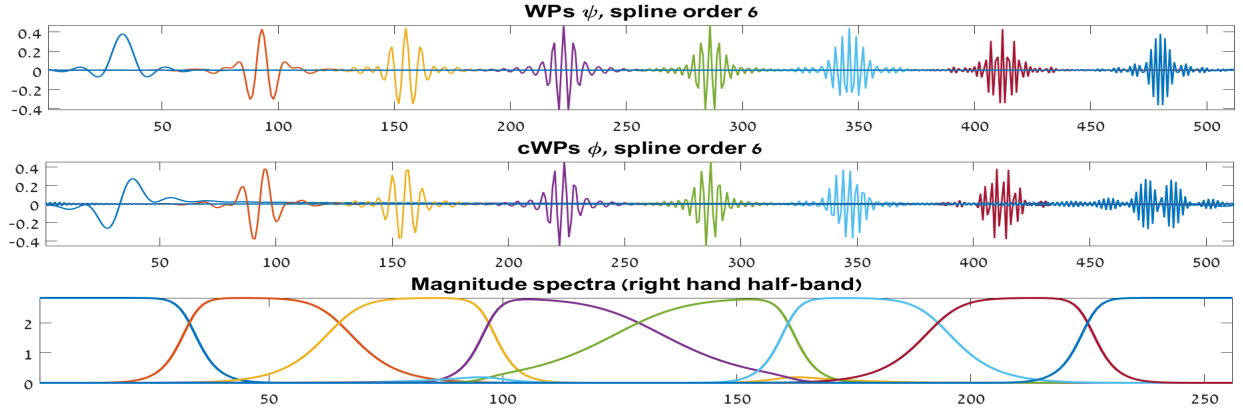


Figure 2.1: Top left to right: third-level dsWPs $\psi_{[3],l}^6$, $l = 0, 1, 2, 3, 4, 5, 6, 7$. Center left to right: third-level cWPs $\varphi_{[3],l}^6$. Bottom: their magnitude of DFT spectra, respectively

2.5 Implementation of qWP transforms

In this section, we briefly outline the implementation scheme, which is described in detail in [1].

2.5.1 One-level transforms

Define the p-filters $\mathbf{q}_{\pm[1]}^l \stackrel{\text{def}}{=} \{q_{\pm[1]}^l[k]\}$, $q_{\pm[1]}^l[k] = \psi_{[1],l}^{2r}[k] \pm i \varphi_{[1],l}^{2r}[k] = \Psi_{\pm[1],l}^{2r}$, $l = 0, 1$. Equation (2.3) implies that their frequency responses are

$$\begin{aligned} \hat{q}_{+[1]}^0[n] &= \begin{cases} (1+i)\sqrt{2}, & \text{if } n = 0; \\ 2\beta[n], & \text{if } 0 < n < N/2; \\ 0 & \text{if } N/2 \leq n < N, \end{cases} & \hat{q}_{+[1]}^1[n] &= \begin{cases} -(1+i)\sqrt{2}, & \text{if } n = N/2; \\ 2\alpha[n], & \text{if } 0 < n < N/2; \\ 0, & \text{if } N/2 < n \leq N. \end{cases} \\ \hat{q}_{-[1]}^0[n] &= \begin{cases} (1-i)\sqrt{2}, & \text{if } n = 0; \\ 2\beta[n], & \text{if } N/2 < n < N, \\ 0 & \text{if } 0 < n \leq N/2; \end{cases} & \hat{q}_{-[1]}^1[n] &= \begin{cases} -(1-i)\sqrt{2}, & \text{if } n = N/2; \\ 2\alpha[n], & \text{if } N/2 < n \leq N; \\ 0, & \text{if } 0 \leq n < N/2, \end{cases} \end{aligned}$$

where $\beta[n] = \frac{\cos^{2r} \frac{\pi n}{N}}{\sqrt{U[n]}}$, $\alpha[n] = \omega^n \beta[n + N/2]$ and $U[n]$ is given in Eq. (2.1). The analysis modulation matrices for the one-level qWP transforms are

$$\tilde{\mathbf{M}}_+^q[n] = \begin{pmatrix} \hat{q}_{+[1]}^0[n] & 0 \\ \hat{q}_{+[1]}^1[n] & -\sqrt{2}(1+i)\delta[n - N/2] \end{pmatrix}, \quad \tilde{\mathbf{M}}_-^q[n] = \begin{pmatrix} (1-i)\sqrt{2}\delta[n] & \hat{q}_{-[1]}^0[n] \\ 0 & \hat{q}_{-[1]}^1[n] \end{pmatrix}, \quad (2.4)$$

The synthesis modulation matrices $\mathbf{M}_{\pm}^q[n] = \tilde{\mathbf{M}}_{\pm}^q[n]$. Application of the matrices $\tilde{\mathbf{M}}_{\pm}^q[n]$ to the vector $(\hat{x}[n], \hat{x}[\vec{n}])^T$ produces the vectors

$$\begin{pmatrix} \hat{z}_{\pm[1]}^0[n] \\ \hat{z}_{\pm[1]}^1[n] \end{pmatrix} = \frac{1}{2}(\tilde{\mathbf{M}}_{\pm}^q[n])^* \cdot \begin{pmatrix} \hat{x}[n] \\ \hat{x}[\vec{n}] \end{pmatrix} = \begin{pmatrix} \hat{y}_{[1]}^0[n] \\ \hat{y}_{[1]}^1[n] \end{pmatrix} \mp i \begin{pmatrix} \hat{c}_{[1]}^0[n] \\ \hat{c}_{[1]}^1[n] \end{pmatrix},$$

where

$$y_{[1]}^{\lambda}[l] = \langle \mathbf{x}, \psi_{[1],\lambda}^{2r}[\cdot - 2l] \rangle, \quad c_{[1]}^{\lambda}[l] = \langle \mathbf{x}, \varphi_{[1],\lambda}^{2r}[\cdot - 2l] \rangle, \quad \vec{n} = n + N/2.$$

Proposition 2.2 ([1]) *Successive application of filter banks defined by the analysis and synthesis modulation matrices $\tilde{\mathbf{M}}_{\pm}^q[n]$ and $\mathbf{M}_{\pm}^q[n]$ to a signal $\mathbf{x} \in \Pi[N]$ produces the analytic signal $\bar{\mathbf{x}}_{\pm}$ associated with \mathbf{x} .*

2.5.2 Multi-level transforms

The transforms with qWPs $\Psi_{\pm[m],l}^{2r}$ from m -th to $m+1$ -th decomposition level ($m \geq 1$) and back are executed by filtering with the same p-filters that are used for the real dsWPs $\psi_{[m],l}^{2r}$.

Proposition 2.3 ([1]) *The DFTs of the qWP transform coefficients from the $m+1$ -th and m -th decomposition levels are linked as follows:*

$$\begin{pmatrix} \hat{z}_{\pm[m+1]}^{\rho 0}[n] \\ \hat{z}_{\pm[m+1]}^{\rho 1}[n] \end{pmatrix} = \frac{1}{2}\tilde{\mathbf{M}}[-2^m n] \cdot \begin{pmatrix} \hat{z}_{\pm[m]}^{\lambda}[n] \\ \hat{z}_{\pm[m]}^{\lambda}[\vec{n}] \end{pmatrix}, \quad \begin{pmatrix} \hat{z}_{\pm[m]}^{\lambda}[n] \\ \hat{z}_{\pm[m]}^{\lambda}[\vec{n}] \end{pmatrix} = \mathbf{M}[2^m n] \cdot \begin{pmatrix} \hat{z}_{\pm[m+1]}^{\rho 0}[n] \\ \hat{z}_{\pm[m+1]}^{\rho 1}[n] \end{pmatrix},$$

where $\rho 0 = \begin{cases} 2\lambda, & \text{if } \lambda \text{ is even;} \\ 2\lambda + 1, & \text{if } \lambda \text{ is odd,} \end{cases}$ and vice versa for $\rho 1$, $\vec{n} = n + N/2^{m+1}$ and $m = 1, \dots, M$.

The modulation matrices $\tilde{\mathbf{M}}[n]$ and $\mathbf{M}[n]$ are defined in Eq. (2.1). By the application of the inverse DFT to the arrays $\{\hat{z}_{\pm[m+1]}^\rho[n]\}$, we get the arrays $\{z_{\pm[m+1]}^\rho[k] = y_{[m+1]}^\rho[k] \pm i c_{[m+1]}^\rho[k]\}$ of the transform coefficients with the qWPs $\Psi_{\pm[m+1],\rho}^{2r}$, where

$$y_{[m+1]}^\rho[k] = \langle \mathbf{x}, \psi_{[m+1],\rho}^{2r}[\cdot - 2^{m+1}k] \rangle, \quad c_{[m+1]}^\rho[k] = \langle \mathbf{x}, \varphi_{[m+1],\rho}^{2r}[\cdot - 2^{m+1}k] \rangle.$$

The transforms are executed in the spectral domain using FFT.

3 Two-dimensional complex wavelet packets

Similarly to the 2D dsWPs $\psi_{[m],j,l}^{2r}[k, n]$, the 2D cWPs $\varphi_{[m],j,l}^{2r}[k, n]$ are defined as the tensor products of 1D WPs such that $\varphi_{[m],j,l}^{2r}[k, n] = \varphi_{[m],j}^{2r}[k] \varphi_{[m],l}^{2r}[n]$. The 2^m -sample shifts of the WPs $\{\varphi_{[m],j,l}^{2r}\}$, $j, l = 0, \dots, 2^m - 1$, in both directions form an orthonormal basis for the space $\Pi[N, N]$ of arrays that are N -periodic in both directions.

3.1 2D complex WPs and their spectra

The 2D dsWPs $\{\psi_{[m],j,l}^{2r}\}$ as well as the cWPs $\{\varphi_{[m],j,l}^{2r}\}$ lack the directionality property which is needed in many applications that process 2D data. However, real-valued 2D wavelet packets oriented in multiple directions can be derived from tensor products of complex quasi-analytic qWPs $\Psi_{\pm[m],\rho}^{2r}$. The complex 2D qWPs are defined as follows:

$$\Psi_{++[m],j,l}^{2r}[k, n] \stackrel{\text{def}}{=} \Psi_{+[m],j}^{2r}[k] \Psi_{+[m],l}^{2r}[n], \quad \Psi_{+-[m],j,l}^{2r}[k, n] \stackrel{\text{def}}{=} \Psi_{+[m],j}^{2r}[k] \Psi_{-[m],l}^{2r}[n],$$

where $m = 1, \dots, M$, $j, l = 0, \dots, 2^m - 1$, and $k, n = -N/2, \dots, N/2 - 1$. The real parts of these 2D qWPs are

$$\begin{aligned} \vartheta_{+[m],j,l}^{2r}[k, n] &\stackrel{\text{def}}{=} \Re(\Psi_{++[m],j,l}^{2r}[k, n]) = \psi_{[m],j,l}^{2r}[k, n] - \varphi_{[m],j,l}^{2r}[k, n], \\ \vartheta_{-[m],j,l}^{2r}[k, n] &\stackrel{\text{def}}{=} \Re(\Psi_{+-[m],j,l}^{2r}[k, n]) = \psi_{[m],j,l}^{2r}[k, n] + \varphi_{[m],j,l}^{2r}[k, n], \end{aligned}$$

The DFT spectra of the 2D qWPs $\Psi_{++[m],j,l}^{2r}$, $j, l = 0, \dots, 2^m - 1$, are the tensor products of the one-sided spectra of the qWPs $\hat{\Psi}_{++[m],j,l}^{2r}[p, q] = \hat{\Psi}_{+[m],j}^{2r}[p] \hat{\Psi}_{+[m],l}^{2r}[q]$ and, as such, they fill the quadrant \mathbf{Q}_0 of the frequency domain, while the spectra of $\Psi_{+-[m],j,l}^{2r}$, $j, l = 0, \dots, 2^m - 1$, fill the quadrant \mathbf{Q}_1 (see Eq. (1.1)). Figure 3.1 displays magnitude spectra of the tenth-order 2D qWPs $\Psi_{++[2],j,l}^{10}$ and $\Psi_{+-[2],j,l}^{10}$ from the second decomposition level.

Figure 3.1 shows that the DFT spectra of the qWPs $\Psi_{\pm[m],j,l}^{10}$ effectively occupy relatively small squares in the frequency domain. For deeper decomposition levels, sizes of the corresponding squares decrease as geometric progression. Such configuration of the spectra leads to the directionality of the real-valued 2D WPs $\vartheta_{\pm[m],j,l}^{2r}$. The directionality of the WPs $\vartheta_{\pm[m],j,l}^{2r}$ is discussed in [1]. It was shown that if the spectrum of a WP $\Psi_{\pm[m],j,l}^{2r}$ occupies a square whose center lies in the point $[\kappa_0, \nu_0]$, then the respective real-valued WP $\vartheta_{\pm[m],j,l}^{2r}$ is represented by $\vartheta_{\pm[m],j,l}^{2r}[k, n] \approx \cos \frac{2\pi(\kappa_0 k + \nu_0 n)}{N} \vartheta[k, n]$, where $\vartheta[k, n]$ is a spatially localized waveform. The spectrum of the 2D signal ϑ comprises only low

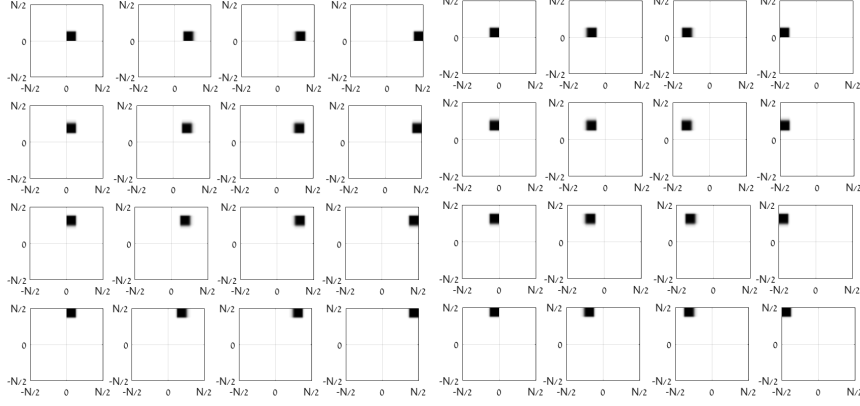


Figure 3.1: Magnitude spectra of 2D qWPs $\Psi_{++[2],j,l}^{10}$ (left) and $\Psi_{+-[2],j,l}^{10}$ (right) from the second decomposition level

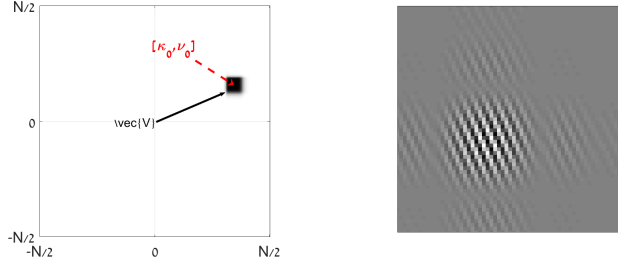


Figure 3.2: Left: magnitude spectra of 2D qWP $\Psi_{++[3],2,5}^{2r}[k,n]$. Right WP $\vartheta_{++[3],2,5}^{2r} = \Re(\Psi_{++[3],2,5}^{2r})$

frequencies in both directions and the signal ϑ does not have a directionality. But the 2D signal $\cos \frac{2\pi(\kappa_0 k + \nu_0 n)}{N}$ is oscillating in the direction of the vector $\vec{V} = \kappa_0 \vec{i} + \nu_0 \vec{j}$. Therefore, WP $\vartheta_{\pm[m],j,l}^{2r}$ can be regarded as the directional cosine modulated by the localized low-frequency signal ϑ . The cosine frequencies in the vertical and horizontal directions are determined by the indices j and l , respectively, of the WP $\vartheta_{\pm[m],j,l}^{2r}$. The bigger is the index, the higher is frequency in the respective direction. The situation is illustrated in Fig. 3.2.

Figures 3.3 and 3.4 display WPs $\vartheta_{+[2],j,l}^{10}$ and $\vartheta_{-[-2],j,l}^{10}$, $j, l = 0, 1, 2, 3$, from the second decomposition level, respectively, and their magnitude spectra

Remark 3.1 Note that the WPs $\vartheta_{+[m],j,l}^{2r}$ and $\vartheta_{+[m],j+1,l+1}^{2r}$ have approximately the same orienta-

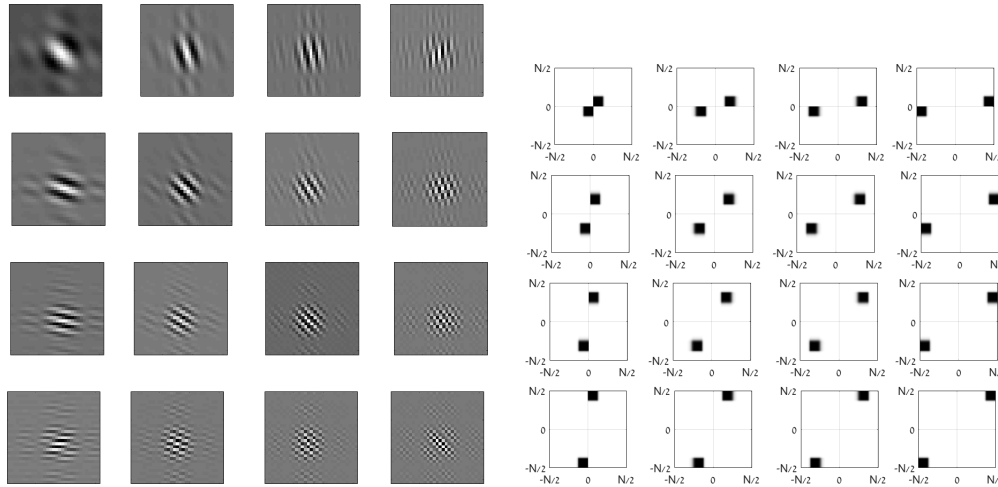


Figure 3.3: WPs $\vartheta_{+[2],j,l}^{10}$ from the second decomposition level and their magnitude spectra

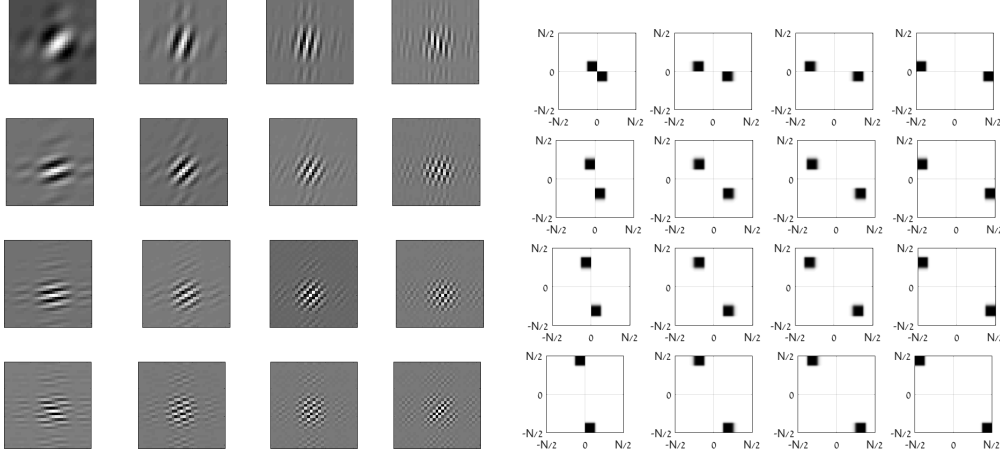


Figure 3.4: WPs $\vartheta_{-[2],j,l}^{10}$ from the second decomposition level and their magnitude spectra

tion. Consequently, the WPs from the m -th decomposition level are oriented in $2^{m+1} - 1$ different directions. The same is true for the WPs $\vartheta_{-[m],j,l}^{2r}$. Thus, at level m , we have waveforms oriented in $2(2^{m+1} - 1)$ directions. It is seen in Figs. 3.3, 3.4.

3.2 Outline of the implementation scheme for 2D qWP transforms

The implementation scheme is described in detail in [1]. The spectra of 1D qWPs $\{\Psi_{+[m],j}^{2r}\}$, $j = 0, \dots, 2^m - 1$, fill the non-negative half-band $[0, N/2]$ and vice versa for the qWPs $\{\Psi_{-[m],j}^{2r}\}$, $j = 0, \dots, 2^m - 1$. Therefore, the spectra of 2D qWPs $\{\Psi_{++[m],j,l}^{2r}\}$, $j, l = 0, \dots, 2^m - 1$ fill the quadrant \mathbf{Q}_0 of the frequency domain (see Eq. (1.1)), while the spectra of 2D qWPs $\{\Psi_{+-[m],j,l}^{2r}\}$ fill the quadrant \mathbf{Q}_1 . Consequently, the spectra of the real-valued 2D WPs $\{\vartheta_{+[m],j,l}^{2r}\}$, $j, l = 0, \dots, 2^m - 1$, and $\{\vartheta_{-[m],j,l}^{2r}\}$ fill the pairs of quadrant $\mathbf{Q}_+ = \mathbf{Q}_0 \cup \mathbf{Q}_2$ and $\mathbf{Q}_- = \mathbf{Q}_1 \cup \mathbf{Q}_3$, respectively.

By this reason, none linear combination of the WPs $\{\vartheta_{+[m],j,l}^{2r}\}$ and their shifts can serve as a basis in the signal space $\Pi[N, N]$. The same is true for WPs $\{\vartheta_{-[m],j,l}^{2r}\}$. However, combinations of the WPs $\{\vartheta_{\pm[m],j,l}^{2r}\}$ provide frames of the space $\Pi[N, N]$.

3.2.1 One-level 2D transforms

The one-level 2D qWP transforms of a signal $\mathbf{X} = \{X[k, n]\} \in \Pi[N, N]$ are implemented by a tensor-product scheme. The following outlines the one-level transforms:

Direct transform with $\Psi_{++[1]}^{2r}$: The 1D transform of columns from the signal \mathbf{X} using the modulation matrix $\tilde{\mathbf{M}}_+^q$ defined in Eq. (2.4), which is followed by the 1D transform of rows of the produced coefficient arrays using the same modulation matrix $\tilde{\mathbf{M}}_+^q$, results in the transform coefficient array $\mathbf{Z}_{+[1]} = \bigcup_{j,l=0}^1 \mathbf{Z}_{+[1]}^{j,l}$, where $Z_{+[1]}^{j,l}[k, n] = \sum_{\lambda,\mu=0}^{N-1} X[\lambda, \mu] \Psi_{++[1],j,l}^{2r}[\lambda - 2k, \mu - 2n]$.

Direct transform with $\Psi_{+-[1]}^{2r}$: The 1D transform of columns from the signal \mathbf{X} using the modulation matrix $\tilde{\mathbf{M}}_+^q$, which is followed by the 1D transform of rows of the produced coefficient

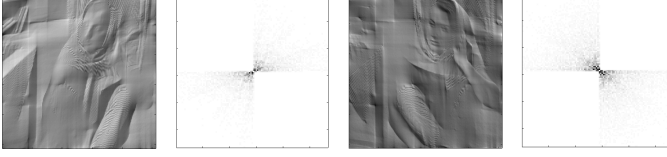


Figure 3.5: Left to right: 1. Image $\Re(\mathbf{X}_+)$. 2. Its magnitude DFT spectrum. 3. Image $\Re(\mathbf{X}_-)$. 4. Its magnitude DFT spectrum

arrays using the modulation matrix $\tilde{\mathbf{M}}_-^q$, results in the array $\mathbf{Z}_{-[1]} = \bigcup_{j,l=0}^1 \mathbf{Z}_{-[1]}^{j,l}$, where $Z_{-[1]}^{j,l}[k, n] = \sum_{\lambda, \mu=0}^{N-1} X[\lambda, \mu] \Psi_{+-[1],j,l}^{2r}[\lambda - 2k, \mu - 2n]$.

Inverse transforms: The complex arrays \mathbf{X}_+ and \mathbf{X}_- are derived from the coefficient arrays $\mathbf{Z}_{+[1]}$ and $\mathbf{Z}_{-[1]}$ using the modulation matrix $\{\mathbf{M}_+^q, \mathbf{M}_+^q\}$ and $\{\mathbf{M}_-^q, \mathbf{M}_+^q\}$, respectively.

The signal \mathbf{X} is restored by $\tilde{\mathbf{X}} = \Re(\mathbf{X}_+ + \mathbf{X}_-)/8$.

Figure 3.5 illustrates the image “Barbara” restoration by the 2D signals $\Re(\mathbf{X}_{\pm})$. The signal $\Re(\mathbf{X}_+)$ captures edges oriented to *north-east*, while $\Re(\mathbf{X}_-)$ captures edges oriented to *north-west*. The signal $\tilde{\mathbf{X}} = \Re(\mathbf{X}_+ + \mathbf{X}_-)/8$ perfectly restores the image achieving PSNR=313.8596 dB.

3.2.2 Multi-level 2D transforms

It was established in Section 2.5.2 that the 1D qWP transforms of a signal $\mathbf{x} \in \Pi[N]$ to the second and further decomposition levels are implemented by the iterated application of the filter banks that are determined by their analysis modulation matrices $\tilde{\mathbf{M}}[2^m n]$, $m = 1, \dots, M-1$, (see Eq. (2.1)) to the coefficient arrays $\mathbf{z}_{\pm[m]}^{\lambda}$. The transforms applied to the arrays $\mathbf{z}_{\pm[m]}^{\lambda}$ produce the arrays $\mathbf{z}_{\pm[m+1]}^{\rho}$, respectively. The inverse transform consists of the iterated application of the filter banks that are determined by their synthesis modulation matrices $\mathbf{M}[2^m n]$, $m = 1, \dots, M-1$, to the coefficient arrays $\mathbf{z}_{\pm[m+1]}^{\rho}$. In that way, the first-level coefficient arrays $\mathbf{z}_{\pm[1]}^{\lambda}$, $\lambda = 0, 1$, are restored.

The 2D transforms of a signal $\mathbf{X} \in \Pi[N, N]$ from m -th to $m+1$ -th decomposition level ($m \geq 1$) consists of the subsequent application of the 1D transforms to columns and rows of the coefficient arrays. The transforms are implemented by application of filter banks, which are determined by the analysis modulation matrix $\tilde{\mathbf{M}}[2^m n]$, to columns and rows of the coefficient arrays $\mathbf{Z}_{\pm[m]}^{j,l}$. The inverse transforms produce the coefficient arrays $\mathbf{Z}_{\pm[1]}^{j,l}$, $j, l = 0, 1$, from which the signal $\mathbf{X} \in \Pi[N, N]$ is restored using the synthesis modulation matrices $\mathbf{M}_{\pm}^q[n]$ as it is explained in Section 3.2.1.

All the computations are implemented in the frequency domain using the FFT. For example, the Matlab execution of the 2D qWP transform of a 512×512 image down to the sixth decomposition level takes 0.45 second. The four-level transform takes 0.20 second.

Summary The 2D qWP processing of a signal $\mathbf{X} \in \Pi[N, N]$ is implemented by a dual-tree scheme. The first step produces two sets $\mathbf{Z}_{+[1]}$ and $\mathbf{Z}_{-[1]}$ of the coefficient arrays which are derived using the analysis modulation matrices $\tilde{\mathbf{M}}_+^q[n]$, and $\tilde{\mathbf{M}}_-^q[n]$, respectively. Further decomposition steps are implemented in parallel on the sets $\mathbf{Z}_{+[1]}$ and $\mathbf{Z}_{-[1]}$ using the same analysis modulation matrix $\tilde{\mathbf{M}}[2^m n]$ for both sets, thus producing two multi-level sets of the coefficient arrays $\{\mathbf{Z}_{+[m]}^{j,l}\}$ and $\{\mathbf{Z}_{-[m]}^{j,l}\}$, $m = 2, \dots, M$, $j, l = 0, 2^m - 1$.

By parallel implementation of the inverse transforms on the coefficients from the sets $\{\mathbf{Z}_{+[m]}^{j,l}\}$ and $\{\mathbf{Z}_{-[m]}^{j,l}\}$ using the same synthesis modulation matrix $\mathbf{M}[2^m n]$, the sets $\mathbf{Z}_{+[1]}$ and $\mathbf{Z}_{-[1]}$ for both sets are restored, which, in turn, provide the signals \mathbf{X}_+ and \mathbf{X}_- , using the synthesis modulation matrices $\mathbf{M}_+^q[n]$ and $\mathbf{M}_-^q[n]$, respectively. Typical signals \mathbf{X}_\pm and their DFT spectra are displayed in Fig. 3.5.

Prior to the reconstruction, some structures, possibly different, are defined in the sets $\{\mathbf{Z}_{+[m]}^{j,l}\}$ and $\{\mathbf{Z}_{-[m]}^{j,l}\}$, $m = 1, \dots, M$, (for example, 2D wavelet, Best Basis or single-level structures) and some manipulations on the coefficients, (for example, thresholding, shrinkage, l_1 minimization) are executed.

4 Image denoising

In this section, we describe application of the directional qWP transforms designed in Section 3 for restoring an image \mathbf{X} from the data $\tilde{\mathbf{X}} = \mathbf{X} + \mathbf{E}$, where \mathbf{E} is the Gaussian zero-mean noise whose STD is σ .

4.1 Denoising scheme for 2D qWPs

The degraded image $\tilde{\mathbf{X}}$ is decomposed into two sets $\{\tilde{\mathbf{Z}}_{+[m]}^{j,l}\}$ and $\{\tilde{\mathbf{Z}}_{-[m]}^{j,l}\}$, $m = 1, \dots, M$, $j, l = 0, 2^m - 1$, of the qWP transform coefficients, then a version of the Bivariate Shrinkage algorithm (BSA)[15, 5] is implemented and the image $\tilde{\mathbf{X}} \approx \mathbf{X}$ is restored from the shrunk coefficients. The image decomposition and reconstruction are explained in Sections 3.2.1 and 3.2.2. The restoration is executed separately from the sets of coefficients belonging to several decomposition levels and the results are averaged with some weights.

4.1.1 Image restoration from a single-level transform coefficients

Consider the estimation of an image $\mathbf{X} \in \Pi[N, N]$ from the fourth-level transform coefficients of the degraded array $\tilde{\mathbf{X}}$ of size $N \times N$.

The denoising algorithm, which we refer to as qWPdn, is implemented by the following steps:

1. In order to eliminate boundary effects, the degraded image $\tilde{\mathbf{X}}$ is symmetrically extended to image $\tilde{\mathbf{X}}_T$ of size $N_1 \times N_1$, where $N_1 = N + 2T$. Typically, $T = N/4$ or $T = N/8$.
2. The Bivariate Shrinkage (BSA) utilizes the interscale dependancy of the transform coefficients. Therefore, the direct 2D transforms of the image $\tilde{\mathbf{X}}_T$ with the complex qWPs Ψ_{++}^{2r} and Ψ_{+-}^{2r} are executed down to the fifth decomposition level. As a result, two sets $\{\tilde{\mathbf{Z}}_{+[m]}^{j,l}\}$ and $\{\tilde{\mathbf{Z}}_{-[m]}^{j,l}\}$, $m = 1, \dots, 5$, $j, l = 0, \dots, 2^m - 1$, of the qWP transform coefficients are produced.
3. The noise variance is estimated by $\tilde{\sigma}_e^2 = \frac{\text{median}(|\tilde{Z}_{+[1]}^{1,1}[k,n]|)}{0.6745}$.
4. $\tilde{c}_4[k, n] \stackrel{\text{def}}{=} \tilde{Z}_{+[4]}^{j,l}[k, n]$ denotes a coefficient from the block $\tilde{\mathbf{Z}}_{+[4]}^{j,l}$ in the fourth decomposition level. The following operations are applied to the coefficient $\tilde{c}_4[k, n]$:

- (a) The averaged variance $\bar{\sigma}_c[k, n]^2 = \frac{1}{W_4^2} \sum_{\kappa, \nu=-W_4/2}^{W_4/2-1} \check{c}_4[k + \kappa, n + \nu]^2$ is calculated. The integer W_4 determines the neighborhood of $\check{c}_4[k, n]$ size.
- (b) The marginal variance for $\check{c}_4[k, n]$ is estimated by $\bar{\sigma}[k, n]^2 = (\bar{\sigma}_c[k, n]^2 - \bar{\sigma}_e^2)_+^2$.
- (c) In order to estimate the clean transform coefficients from the fourth decomposition level, it is needed to utilize the coefficients from the fifth level. The size of the coefficient block $\check{\mathbf{Z}}_{+[4]}^{j,l}$ is $N_1/16 \times N_1/16$. The coefficients from that block are related to the qWP $\Psi_{++[4],j,l}^{2r}$, whose spectrum occupies, approximately, a square $\mathbf{S}_{+[4]}^{j,l}$ of size $N_1/32 \times N_1/32$ within the quadrant \mathbf{Q}_0 . The spectrum's location determines the directionality of the waveform $\Psi_{++[4],j,l}^{2r}$. On the other hand, four coefficient blocks $\{\check{\mathbf{Z}}_{+[5]}^{2j+\iota, 2l+\lambda}\}$, $\iota, \lambda = 0, 1$, of size $N_1/32 \times N_1/32$ are derived by filtering the block $\check{\mathbf{Z}}_{+[4]}^{j,l}$ followed by downsampling. The coefficients from those blocks are related to the qWPs $\Psi_{++[5], 2j+\iota, 2l+\lambda}^{2r}$, whose spectra occupy, approximately, the squares $\mathbf{S}_{+[5]}^{2j+\iota, 2l+\lambda}$ of size $N_1/64 \times N_1/64$, which fill the square $\mathbf{S}_{+[4]}^{j,l}$. Therefore, the orientations of the waveforms $\Psi_{++[5], 2j+\iota, 2l+\lambda}^{2r}$ are close to the orientation of $\Psi_{++[4],j,l}^{2r}$. Keeping this in mind, we form the joint fifth-level array $\mathbf{c}_5^{j,l}$ of size $N_1/16 \times N_1/16$ by interleaving the coefficients from the arrays $\{\check{\mathbf{Z}}_{+[5]}^{2j+\iota, 2l+\lambda}\}$. To be specific, the joint array $\mathbf{c}_5^{j,l}$ consists of the quadruples:

$$\mathbf{c}_5^{j,l} = \left\{ \begin{bmatrix} \check{Z}_{+[5]}^{2j, 2l}[\kappa, \nu] & \check{Z}_{+[5]}^{2j, 2l+1}[\kappa, \nu] \\ \check{Z}_{+[5]}^{2j+1, 2l}[\kappa, \nu] & \check{Z}_{+[5]}^{2j+1, 2l+1}[\kappa, \nu] \end{bmatrix} \right\}, \quad \kappa, \nu = 0, \dots, N_1/32 - 1.$$

- (d) Let $\check{c}_5[k, n]$ denote a coefficient from the joint array $\mathbf{c}_5^{j,l}$. Then, the transform coefficient $Z_{+[4]}^{j,l}[k, n]$ from the fourth decomposition level is estimated by the bivariate shrinkage of the coefficients $\check{Z}_{+[4]}^{j,l}[k, n]$:

$$Z_{+[4]}^{j,l}[k, n] \approx \tilde{Z}_{+[4]}^{j,l}[k, n] = \frac{\left(\sqrt{\check{c}_4[k, n]^2 + \check{c}_5[k, n]^2} - \frac{\sqrt{3}\bar{\sigma}_e^2}{\bar{\sigma}[k, n]} \right)_+}{\sqrt{\check{c}_4[k, n]^2 + \check{c}_5[k, n]^2}} \check{c}_4[k, n].$$

5. As a result of the above operations, the fourth-level coefficient array $\tilde{\mathbf{Z}}_{+[4]} = \{\tilde{\mathbf{Z}}_{+[4],j,l}\}$, $j, l = 0, \dots, 15$, is estimated, where $\tilde{\mathbf{Z}}_{+[4],j,l} = \{\tilde{Z}_{+[4]}^{j,l}[k, n]\}$, $k, n = 0, \dots, N_1/16 - 1$.
6. The inverse qWP transform is applied to the coefficient array $\tilde{\mathbf{Z}}_{+[4]}$ and the result shrinks to the original image size $N \times N$. Thus, the sub-image $\tilde{\mathbf{X}}_+^4$ is obtained.
7. The same operations are applied to $\check{\mathbf{Z}}_{-[m]}^{j,l}$, $m = 4, 5$, thus resulting in the sub-image $\tilde{\mathbf{X}}_-^4$.
8. The clean image is estimated by $\mathbf{X} \approx \tilde{\mathbf{X}}^4 = \frac{\Re(\tilde{\mathbf{X}}_+^4 + \tilde{\mathbf{X}}_-^4)}{8}$.

² $s_+ \stackrel{\text{def}}{=} \max\{s, 0\}$.

4.1.2 Image restoration from several decomposition levels

More stable estimation of the image \mathbf{X} is derived by the weighted average of several single-level estimations $\{\tilde{\mathbf{X}}^m\}$. In most cases, the estimations from the second, third and fourth levels are combined, so that $m = 2, 3, 4$.

The approximated image $\tilde{\mathbf{X}}^3$ is derived from the third-level coefficients $\tilde{\mathbf{Z}}_{\pm[3]}^{j,l}$. The fourth-level coefficients that are needed for the Bivariate Shrinkage of the coefficients $\tilde{\mathbf{Z}}_{\pm[3]}^{j,l}$ are taken from the “cleaned” arrays $\tilde{\mathbf{Z}}_{\pm[4],j,l}$ rather than from the “raw” ones $\tilde{\mathbf{Z}}_{\pm[4],j,l}$.

Similarly, the image $\tilde{\mathbf{X}}^2$, is derived from the coefficient arrays $\tilde{\mathbf{Z}}_{\pm[2]}^{j,l}$ and $\tilde{\mathbf{Z}}_{\pm[3]}^{j,l}$. The final operation is the weighted averaging such as

$$\tilde{\mathbf{X}} = \frac{\alpha_2 \tilde{\mathbf{X}}^2 + \alpha_3 \tilde{\mathbf{X}}^3 + \alpha_4 \tilde{\mathbf{X}}^4}{\alpha_2 + \alpha_3 + \alpha_4}. \quad (4.1)$$

Remark 4.1 *Matlab implementation of all the operations needed to transform the degraded array $\tilde{\mathbf{X}}$ of size 512×512 into the estimation $\tilde{\mathbf{X}}$ given by Eq. (4.1) takes 1 second. Note that the noise STD is not a part of the input. It is evaluated as indicated in Item 3.*

Remark 4.2 *In some cases, restoration from third, fourth and fifth levels is preferable. Then, the degraded array $\tilde{\mathbf{X}}_T$ is decomposed down to the sixth level.*

Remark 4.3 *The algorithm comprises a number of free parameters which enable a flexible adaptation to the processed object. These parameters are the order $2r$ of the generating discrete spline, integers W_4 and W_3 and W_2 , which determine the sizes of neighborhoods for the averaged variances calculation, and the weights α_2 , α_3 and α_4 .*

Remark 4.4 *Fragments of the Matlab functions `denoising_dwt.m` and `bishrink.m` from the web-sites http://eeweb.poly.edu/iselesni/WaveletSoftware/denoising_dwt.html and <http://eeweb.poly.edu/iselesni/WaveletSoftware/denoise2.html>, respectively, were used as patterns while compiling our own denoising software.*

4.2 qWPdn–BM3D: Hybrid algorithm

Experiments with the qWPdn image denoising demonstrate its ability to restore edges and texture details even from severely degraded images. Certainly, this ability stems from the fact that the designed in Section 3.1 2D qWP transforms provide a variety of 2D waveforms oriented in multiple directions, which are spatially localized and have oscillatory structure. In most conducted experiments, the qWPdn provides better resolution of edges and fine structures compared to the cptTP-CTF₆, DAS-2 and BM3D algorithms, which is reflected in higher SSIM values. On the other hand, the BM3D algorithm proved to be superior in noise suppression especially in smooth regions in images, thus producing the highest PSNR values in almost all the experiments. However, some over-smoothing effect on the edges and fine texture persisted with the application of the BM3D algorithm. Especially, this was the case for severely degraded images.

In this section, we propose to combine qWPdn with BM3D algorithms to benefit from the strong features of both algorithms.

Denote by \mathbf{Q} and \mathbf{B} the operators of application of the qWPdn and BM3D denoising algorithms, respectively, to a degraded array \mathbf{A} : $\mathbf{Q}\mathbf{A} = \mathbf{D}_Q$ and $\mathbf{B}\mathbf{A} = \mathbf{D}_B$.

Assume that we have an array $\tilde{\mathbf{X}}^0 = \mathbf{X} + \mathbf{E}$, which represents an image \mathbf{X} degraded by additive Gaussian noise \mathbf{E} whose STD is σ . The denoising processing is implemented along with the following scheme.

First step: Apply the operators \mathbf{Q} and \mathbf{B} to the input array $\tilde{\mathbf{X}}^0$: $\mathbf{Y}_Q^1 = \mathbf{Q} \tilde{\mathbf{X}}^0$ and $\mathbf{Y}_B^1 = \mathbf{B} \tilde{\mathbf{X}}^0$.

Iterations: $i = 1, \dots, I - 1$

1. Form new input arrays $\tilde{\mathbf{X}}_Q^i = \frac{\tilde{\mathbf{X}}^0 + \mathbf{Y}_Q^i}{2}$, $\tilde{\mathbf{X}}_B^i = \frac{\tilde{\mathbf{X}}^0 + \mathbf{Y}_B^i}{2}$.
2. Apply the operators \mathbf{Q} and \mathbf{B} to the new input arrays: $\mathbf{Y}_Q^{i+1} = \mathbf{Q} \tilde{\mathbf{X}}_B^i$, $\mathbf{Y}_B^{i+1} = \mathbf{B} \tilde{\mathbf{X}}_Q^i$.

Estimations of the clean image: Three estimations are used:

1. The updated BM3D estimation $\tilde{\mathbf{X}}_{uB} \stackrel{\text{def}}{=} \mathbf{Y}_B^I$ (**upBM3D**).
2. The updated qWPdn estimation $\tilde{\mathbf{X}}_{uQ} \stackrel{\text{def}}{=} \mathbf{Y}_Q^I$ (**upqWP**).
3. The hybrid estimation $\tilde{\mathbf{X}}_H \stackrel{\text{def}}{=} (\mathbf{Y}_B^I + \mathbf{Y}_Q^I)/2$ (**hybrid**).

4.3 Experimental results

In this section, we compare the performance of our denoising schemes designated as **upBM3D**, **upqWP** and **hybrid** on the restoration of degraded images with the performances of the state-of-the-art algorithms such as cptTP-CTF₆, **DAS-2** and, especially, **BM3D**. To produce results for the comparison, we used the software available at the websites http://www.cs.tut.fi/~foi/GCF-BM3D/index.html#ref_software (BM3D) and <http://staffweb1.cityu.edu.hk/xzhuang7/softs/index.html#bdTPCTF> (cptTP-CTF₆ and DAS-2).

The restored images were evaluated by the visual perception, by Peak Signal-to-Noise ratio (PSNR) (see Eq. (4.2))³ and by the Structural Similarity Index (SSIM) ([16], `ssim.m` Matlab function). The SSIM measures the structural similarity of small moving windows in two images. It varies from 1 for fully identical windows to -1 for completely dissimilar ones. The SSIM map visualizes the local index values for all the images' pixels while the global index is the average of the local indices. Currently, the SSIM is regarded as more informative characteristics of the image quality compared to PSNR and Mean Square Error (MSE).

For the experiments, we used a standard set of benchmark images: "Lena", "Boat", "Goldhill", "Barbara" and "Mandrill" and one image that represents a stacked seismic section designated as "Seismic". The "clean" images are displayed in Fig. 4.1. The images were corrupted by Gaussian zero-mean noise whose STD was $\sigma = 5, 10, 25, 40, 50, 80, 100$ dB. Then, the **BM3D**, **upBM3D**, **upqWP**, **hybrid**, cptTP-CTF₆ and **DAS-2** denoising algorithms were applied to restore the images. In most experiments the algorithm **upBM3D** performed better than **upqWP**. However, this was not the case in experiments with the "Seismic" image. Therefore, in the "Seismic" block in Table 4.1 and pictures in Fig. 4.2, we provide results from experiments with **upqWP** rather than with **upBM3D** algorithm.

3

$$PSNR(\mathbf{x}, \tilde{\mathbf{x}}) \stackrel{\text{def}}{=} 10 \log_{10} \left(\frac{K 256^2}{\sum_{k=1}^K (x_k - \tilde{x}_k)^2} \right) dB. \quad (4.2)$$

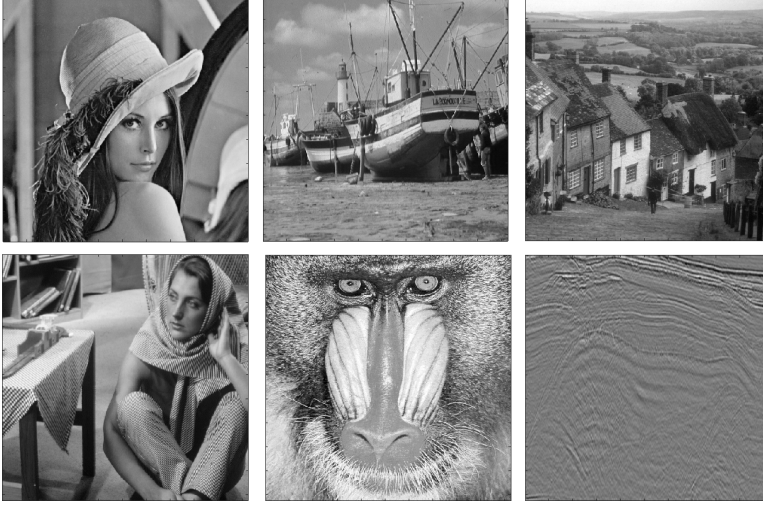


Figure 4.1: Clean images: “Lena”, “Boat”, “Goldhill”, “Barbara”, “Mandrill” and “Seismic”

Table 4.1 summarizes the experimental results from the restoration of “Barbara”, “Seismic” and “Boat” images corrupted by additive Gaussian noise. PSNR and SSIM values for each experiment are given.

The diagrams in Fig. 4.2 illustrate the results reported in Table 4.1.

Figure 4.3 displays fragments of the “Seismic” image corrupted by Gaussian noise with STD $\sigma = 40$ dB and of the image restored by the **BM3D**, **upqWP** and **hybrid** algorithms. It is seen that most part of the image structure is lost by **BM3D** restoration which is not the case for the **hybrid** and, especially, the **upqWP** algorithms. This fact is reflected in the SSIM values which are 0.4432 and 0.3606 by **upqWP** and **BM3D**, respectively.

Figure 4.4 displays the “Barbara” image corrupted by Gaussian noise with STD $\sigma = 50$ dB and the image restored by the **BM3D**, **upBM3D** and **hybrid** algorithms. One can observe that the **BM3D** restoration produces over-smoothing of some parts of the image compared to the restoration by the **hybrid** and, especially, by the **upBM3D** algorithms. It is clearly seen in Fig. 4.5 which displays fragment of the above images. The the SSIM values which are 0.5619 and 0.5389 for **upBM3D** and **BM3D**, respectively.

Table 4.2 summarizes the experimental results on the restoration of the “Lena”, “Mandrill” and “Goldhill” images corrupted by additive Gaussian noise. The PSNR and SSIM values for each experiment are given. Diagrams in Fig. 4.6 illustrate these results.

Figure 4.7 displays the “Mandrill” image corrupted by strong Gaussian noise with STD $\sigma = 80$ dB and the image restored by the **BM3D**, **upBM3D** and **hybrid** algorithms. **BM3D** restoration, although achieving the highest PSNR value, produces a number of smeared spots in the image, which is not the case with **upBM3D** and, especially, with the **hybrid**. This fact is reflected in the SSIM values which are 0.3361 and 0.2459 for **hybrid** and **BM3D**, respectively.

Figure 4.8 displays fragments of the “Goldhill” image corrupted by Gaussian noise with STD $\sigma = 50$ dB and of the image restored by **BM3D**, **upBM3D** and **hybrid** algorithms. It is seen that some parts of the image structure (roofs, windows, ground) are over-smoothed by the **BM3D** restoration compared to the **hybrid** and the **upBM3D** restorations. This fact is reflected in the SSIM values which are 0.4122 and 0.3825 for **hybrid** and **BM3D**, respectively.

σ	5	10	25	40	50	80	100
Barbara							
noised	<u>34.19</u> <u>0.77</u>	<u>28.17</u> <u>0.6</u>	<u>20.21</u> <u>0.35</u>	<u>16.13</u> <u>0.23</u>	<u>14.19</u> <u>0.18</u>	<u>10.11</u> <u>0.09</u>	<u>8.17</u> <u>0.06</u>
cptTP-CTF ₆	<u>37.75</u> <u>0.8382</u>	<u>34.07</u> <u>0.763</u>	<u>29.28</u> <u>0.6358</u>	<u>26.78</u> <u>0.5375</u>	<u>25.64</u> <u>0.4833</u>	<u>23.47</u> <u>0.3633</u>	<u>22.59</u> <u>0.3092</u>
DAS-2	<u>37.75</u> <u>0.8438</u>	<u>34.01</u> <u>0.764</u>	<u>29.43</u> <u>0.6422</u>	<u>27.13</u> <u>0.5595</u>	<u>26.04</u> <u>0.5121</u>	<u>23.76</u> <u>0.3987</u>	<u>22.67</u> <u>0.3398</u>
BM3D	<u>38.34</u> <u>0.8387</u>	<u>35.01</u> <u>0.7738</u>	30.75 <u>0.6707</u>	<u>28.02</u> <u>0.5788</u>	<u>27.26</u> <u>0.5389</u>	<u>24.82</u> <u>0.4192</u>	<u>23.66</u> <u>0.3608</u>
upBM3D	<u>38.44</u> 0.8531	<u>34.88</u> <u>0.7846</u>	<u>30.65</u> 0.6806	28.42 0.6062	27.32 0.5619	<u>24.78</u> <u>0.4396</u>	23.92 <u>0.39</u>
Hybrid	38.51 <u>0.8494</u>	35.02 0.7847	<u>30.69</u> <u>0.6792</u>	<u>28.34</u> <u>0.6021</u>	<u>27.28</u> <u>0.5581</u>	24.9 0.4449	<u>23.9</u> 0.3912
Seismic							
noised	<u>34.19</u> <u>0.8</u>	<u>28.17</u> <u>0.55</u>	<u>20.21</u> <u>0.22</u>	<u>16.13</u> <u>0.12</u>	<u>14.19</u> <u>0.08</u>	<u>10.11</u> <u>0.04</u>	<u>8.17</u> <u>0.03</u>
cptTP-CTF ₆	<u>38.844</u> <u>0.9107</u>	<u>34.87</u> <u>0.7696</u>	<u>30.75</u> <u>0.4616</u>	<u>29.14</u> <u>0.3188</u>	<u>28.43</u> <u>0.2618</u>	<u>26.95</u> <u>0.1616</u>	<u>26.2</u> <u>0.127</u>
DAS-2	<u>38.84</u> <u>0.9141</u>	<u>34.86</u> <u>0.795</u>	<u>30.7</u> <u>0.5383</u>	<u>28.91</u> <u>0.3938</u>	<u>28.08</u> <u>0.3318</u>	<u>26.26</u> <u>0.2222</u>	<u>25.32</u> <u>0.1785</u>
BM3D	<u>39.03</u> <u>0.9126</u>	<u>34.94</u> <u>0.77</u>	<u>30.84</u> <u>0.4984</u>	<u>29.11</u> <u>0.3606</u>	<u>28.48</u> <u>0.2853</u>	27.01 <u>0.19</u>	26.34 <u>0.1547</u>
upqWP	39.51 0.929	35.47 0.8294	<u>31.01</u> 0.5822	<u>28.85</u> 0.4437	<u>28.35</u> 0.3838	<u>26.53</u> 0.2809	<u>25.84</u> 0.2376
Hybrid	<u>39.37</u> <u>0.9266</u>	<u>35.41</u> <u>0.8219</u>	31.1 <u>0.57</u>	29.22 <u>0.4341</u>	28.56 <u>0.3715</u>	<u>26.89</u> <u>0.2696</u>	<u>26.28</u> <u>0.2244</u>
Boat							
noised	<u>34.19</u> <u>0.79</u>	<u>28.17</u> <u>0.58</u>	<u>20.21</u> <u>0.29</u>	<u>16.13</u> <u>0.18</u>	<u>14.19</u> <u>0.13</u>	<u>10.11</u> <u>0.07</u>	<u>8.17</u> <u>0.05</u>
cptTP-CTF ₆	<u>36.89</u> <u>0.8044</u>	<u>33.38</u> <u>0.6713</u>	<u>29.16</u> <u>0.504</u>	<u>27.05</u> <u>0.4044</u>	<u>26.12</u> <u>0.3567</u>	<u>24.31</u> <u>0.2626</u>	<u>23.52</u> <u>0.2232</u>
DAS-2	<u>36.89</u> <u>0.8294</u>	<u>33.18</u> <u>0.688</u>	<u>28.92</u> <u>0.5182</u>	<u>26.81</u> <u>0.4228</u>	<u>25.85</u> <u>0.3763</u>	<u>23.87</u> <u>0.2792</u>	<u>22.93</u> <u>0.2361</u>
BM3D	37.32 <u>0.8065</u>	33.95 <u>0.6805</u>	29.94 <u>0.5296</u>	<u>27.77</u> <u>0.4395</u>	<u>26.81</u> <u>0.3899</u>	<u>24.896</u> <u>0.2952</u>	<u>24</u> <u>0.2533</u>
upBM3D	<u>37.26</u> 0.8315	<u>33.92</u> <u>0.7016</u>	<u>29.89</u> <u>0.548</u>	27.81 0.46	26.89 0.4148	24.903 <u>0.3185</u>	24.07 <u>0.2766</u>
Hybrid	<u>37.11</u> <u>0.8165</u>	<u>33.81</u> 0.7049	<u>29.69</u> 0.5505	<u>27.61</u> <u>0.4587</u>	<u>26.66</u> <u>0.4137</u>	<u>24.82</u> 0.3191	<u>23.96</u> 0.2777

Table 4.1: $\frac{PSNR}{SSIM}$ values for restoration of “Barbara”, “Seismic” and “Boat” images. Boldface highlights the best results

σ	5	10	25	40	50	80	100
Lena							
noised	<u>34.19</u> 0.65	<u>28.17</u> 0.43	<u>20.21</u> 0.2	<u>16.13</u> 0.12	<u>14.19</u> 0.09	<u>10.11</u> 0.04	<u>8.17</u> 0.03
cptTP-CTF ₆	<u>38.4</u> 0.705	<u>35.49</u> 0.616	<u>31.56</u> 0.4992	<u>29.45</u> 0.4313	<u>28.45</u> 0.3965	<u>26.39</u> 0.3199	<u>25.45</u> 0.2833
DAS-2	<u>38.21</u> 0.7272	<u>35.24</u> 0.625	<u>31.12</u> 0.4920	<u>28.94</u> 0.4148	<u>27.87</u> 0.3757	<u>25.56</u> 0.29	<u>24.43</u> 0.2485
BM3D	<u>38.75</u> 0.7078	35.96 0.6233	32.11 0.5026	<u>29.9</u> 0.4265	29.08 0.3957	27.01 0.3214	25.99 0.2851
upBM3D	<u>38.76</u> 0.7405	<u>35.8</u> 0.6434	<u>32.03</u> 0.5143	29.94 0.4423	<u>29</u> 0.4088	<u>26.84</u> 0.3316	<u>25.98</u> 0.3008
Hybrid	38.79 0.733	<u>35.86</u> 0.6439	<u>31.88</u> 0.517	<u>29.75</u> 0.4451	<u>28.83</u> 0.4127	<u>26.75</u> 0.338	<u>25.87</u> 0.305
Mandrill							
noised	<u>34.19</u> 0.7	<u>28.17</u> 0.52	<u>20.21</u> 0.51	<u>16.13</u> 0.34	<u>14.19</u> 0.26	<u>10.11</u> 0.14	<u>8.17</u> 0.1
cptTP-CTF ₆	<u>35.09</u> 0.9252	<u>30.36</u> 0.8198	<u>25.34</u> 0.6082	<u>23.19</u> 0.4531	<u>22.28</u> 0.371	<u>20.76</u> 0.2148	<u>20.23</u> 0.1617
DAS-2	<u>35.05</u> 0.9303	<u>30.28</u> 0.8329	<u>25.27</u> 0.64	<u>23.23</u> 0.51	<u>22.38</u> 0.4423	<u>20.83</u> 0.2997	<u>20.18</u> 0.2376
BM3D	35.1 0.9209	<u>30.38</u> 0.8135	<u>25.31</u> 0.6095	<u>23.03</u> 0.4613	<u>22.31</u> 0.3813	20.93 0.2459	<u>20.42</u> 0.1956
upBM3D	<u>34.57</u> 0.9131	30.43 0.8372	25.47 0.6541	23.43 0.5353	22.54 0.4754	<u>20.82</u> 0.3223	20.56 0.2459
Hybrid	<u>33.4</u> 0.8914	<u>30.08</u> 0.8301	<u>25.47</u> 0.6536	<u>23.42</u> 0.5381	<u>22.53</u> 0.4803	<u>20.85</u> 0.3361	<u>20.51</u> 0.2549
Goldhill							
noised	<u>34.19</u> 0.8	<u>28.17</u> 0.59	<u>20.21</u> 0.27	<u>16.13</u> 0.15	<u>14.19</u> 0.11	<u>10.11</u> 0.05	<u>8.17</u> 0.03
cptTP-CTF ₆	<u>36.86</u> 0.8388	<u>33.21</u> 0.7157	<u>29.17</u> 0.4992	<u>27.4</u> 0.3903	<u>26.62</u> 0.3425	<u>25.04</u> 0.2495	<u>24.32</u> 0.2108
DAS-2	<u>36.71</u> 0.8447	<u>33.06</u> 0.7292	<u>29.18</u> 0.5327	<u>27.35</u> 0.4245	<u>26.5</u> 0.3747	<u>24.66</u> 0.2733	<u>23.73</u> 0.2272
BM3D	<u>37.17</u> 0.8384	<u>33.65</u> 0.7193	<u>29.88</u> 0.5311	<u>28.02</u> 0.4305	<u>27.23</u> 0.3825	<u>25.46</u> 0.2878	<u>24.62</u> 0.2448
upBM3D	37.2 0.8525	33.7 0.7472	29.91 0.5626	28.1 0.459	27.29 0.4094	25.52 0.311	24.75 0.2686
Hybrid	<u>36.04</u> 0.8504	<u>33.58</u> 0.7489	<u>29.74</u> 0.567	<u>27.96</u> 0.4623	<u>27.17</u> 0.4122	<u>25.51</u> 0.3132	<u>24.72</u> 0.2701

Table 4.2: $\frac{PSNR}{SSIM}$ values for restoration of “Lena”, “Mandrill” and “Goldhill” images. Boldface highlights the best results

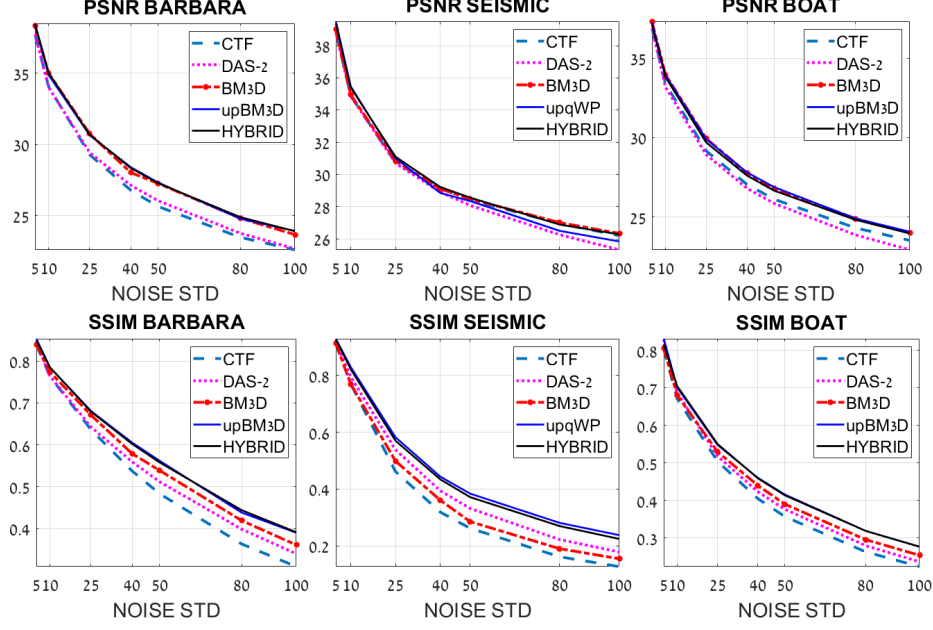


Figure 4.2: Diagrams of PSNR and SSIM values for restoration of “Barbara”, “Seismic” and “Boat” images

5 Discussion

We presented denoising schemes that combine the qWPdn algorithm based on the directional quasi-analytic wavelet packets, which are designed in [1], with the popular BM3D algorithm [6], considered to be one of the best in the field. Either of the two methods have their strong features and shortcomings. The qWPdn method described in Section 4.1 demonstrates the ability to restore edges and texture details even from severely degraded images. This ability stems from the fact that the designed 2D qWP transforms provide a variety of 2D waveforms, which are close to windowed cosines with multiple frequencies oriented in multiple directions. In most conducted experiments, the qWPdn method provided better resolution of edges and fine structures compared to what cptTP-CTF₆, DAS-2 and BM3D algorithms, which were reflected by the higher SSIM values. In turn, the BM3D algorithm is superior for noise suppression, especially in smooth regions in images, thus producing the highest PSNR values in almost all the experiments. However, some over-smoothing effect on the edges and fine texture are persisted with the BM3D algorithm.

qWPdn and BM3D methods complement each other. Therefore, the idea to combine these methods is natural. The iterative hybrid scheme qWPdn–BM3D proposed in Section 4.2, where the output from one algorithm updates the input to the other, proved to be highly efficient. In the overwhelming majority of the experiments reported in Section 4.3 (and in many others), the two combined algorithms produce higher PSNR values than or very close to the values produced by BM3D. Their noise suppression efficiency is competitive with that of the BM3D. On the other hand, their performance in the resolution of edges and fine structures is much better than the BM3D performance by itself. Consequently, the SSIM values produced by the combined algorithms qWPdn–BM3D were significantly higher than the values produced by BM3D. In all the experiments except for one, the performance of the cptTP-CTF₆ and DAS-2 algorithms was inferior to that of

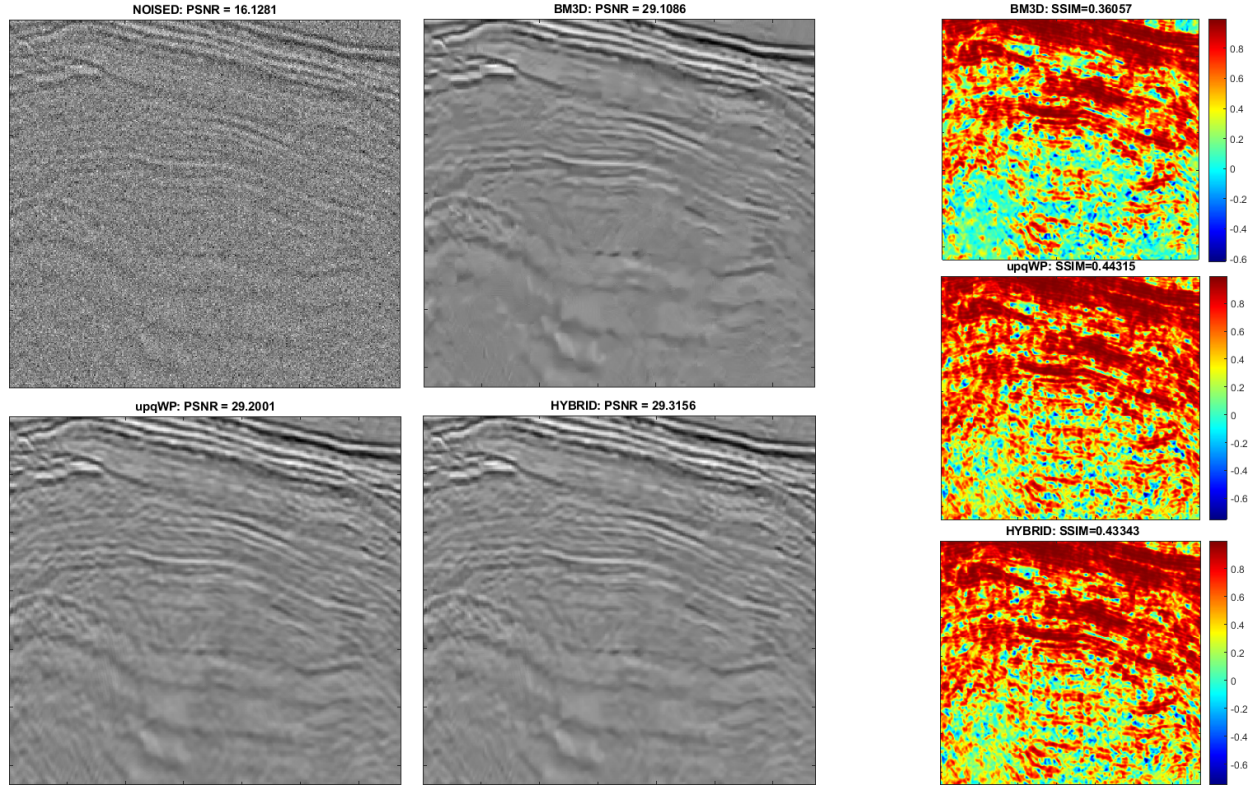


Figure 4.3: Restoration of “Seismic” image corrupted by Gaussian noise with STD $\sigma = 40$ dB. Left panel: Top left: fragment of corrupted image, PSNR=16.13 dB. Top right: fragment of image restored by **BM3D**, PSNR=29.11 dB. Bottom left: fragment of image restored by **upqWP**, PSNR=29.2 dB. Bottom right: fragment of image restored by **hybrid**, PSNR=29.32 dB. Right panel: Top: fragment of SSIM map for **BM3D**, SSIM=0.3606. Center: fragment of SSIM map for **upqWP**, SSIM=0.4432. Bottom: fragment of SSIM map for **hybrid**, SSIM=0.4334

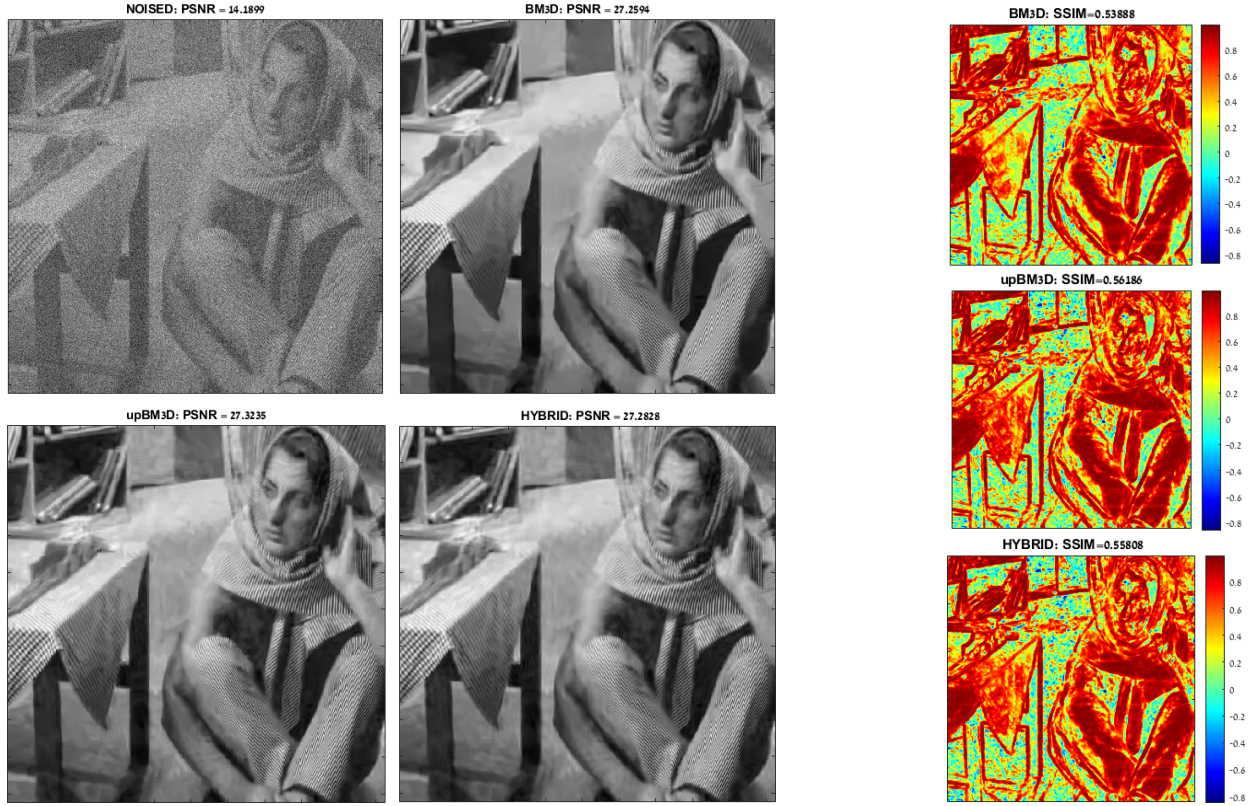


Figure 4.4: Restoration of "Barbara" image corrupted by Gaussian noise with STD $\sigma = 50$ dB. Left panel: Top left: corrupted image, PSNR=14.19 dB. Top right: image restored by **BM3D**, PSNR=27.26 dB. Bottom left: image restored by **upBM3D**, PSNR=27.33 dB. Bottom right: image restored by **hybrid**, PSNR=27.28 dB. Right panel: Top: SSIM map for **BM3D**, SSIM=0.5389. Center: SSIM map for **upBM3D**, SSIM=0.5619. Bottom: SSIM map for **hybrid**, SSIM=0.5581

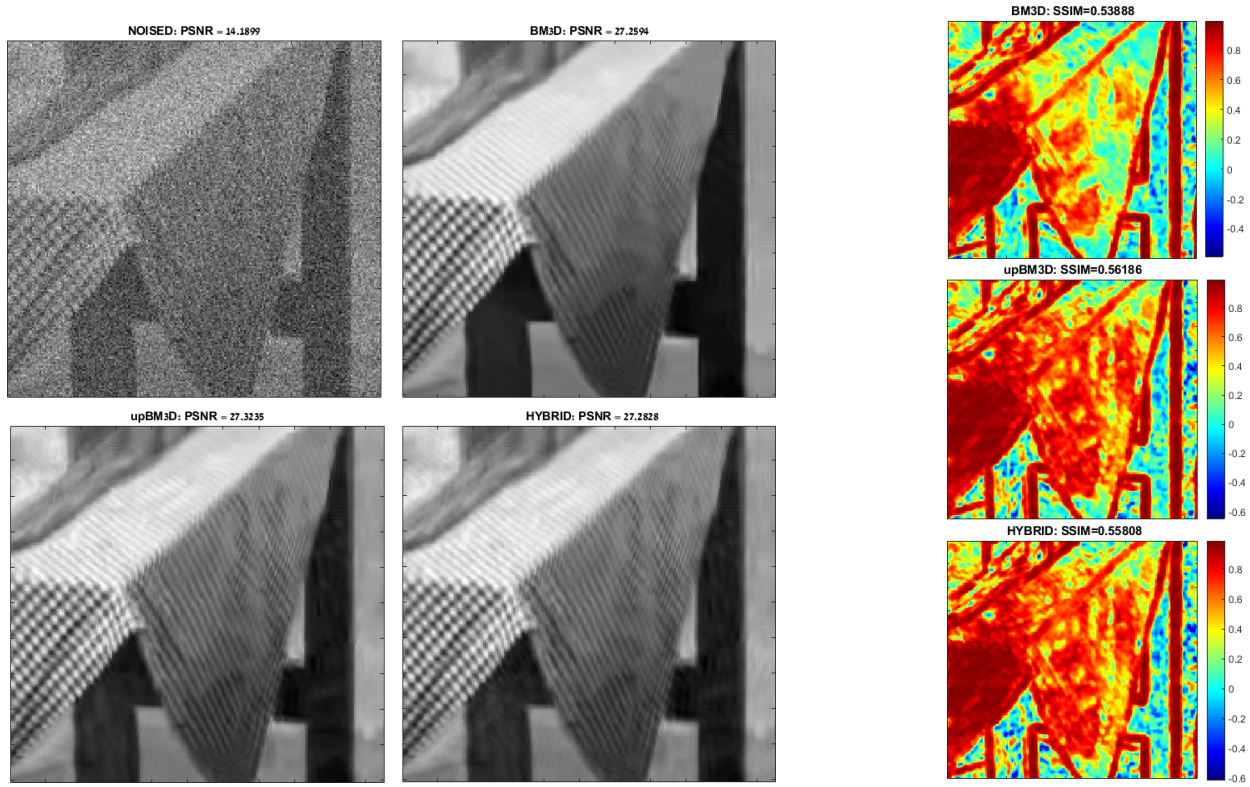


Figure 4.5: Fragments of images displayed in Fig. 4.4

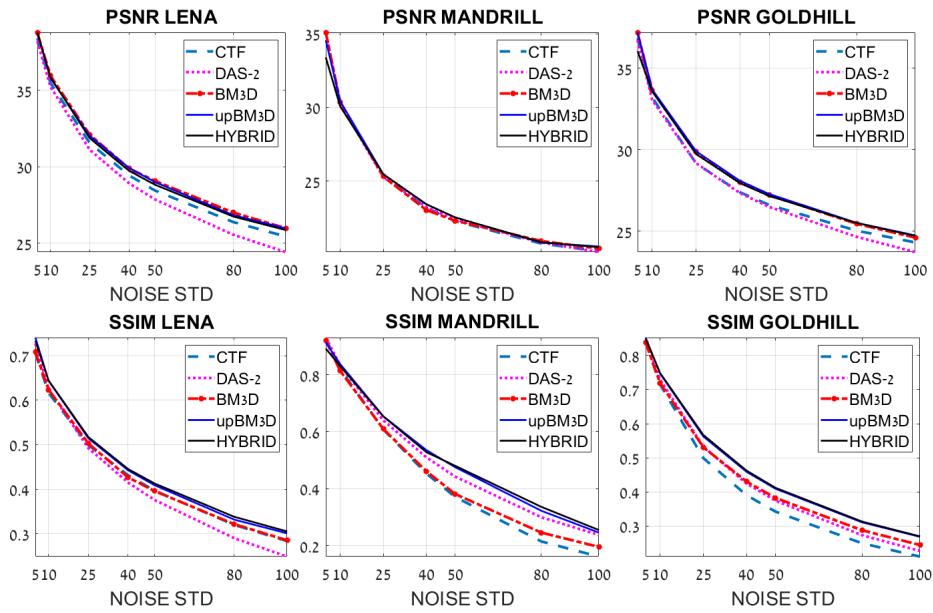


Figure 4.6: Diagrams of PSNR and SSIM values for restoration of “Lena”, “Mandrill” and “Goldhill” images

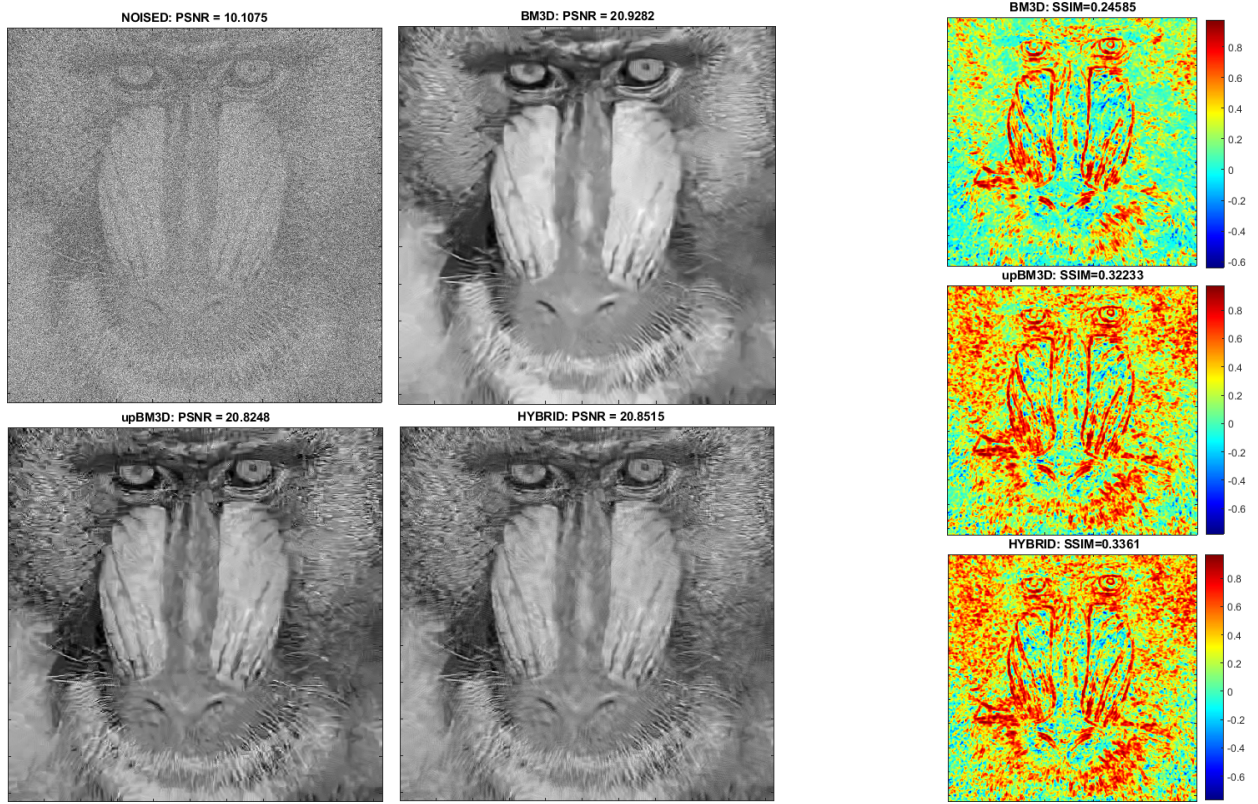


Figure 4.7: Restoration of “Mandrill” image corrupted by Gaussian noise with STD $\sigma = 80$ dB. Left panel: Top left: corrupted image, PSNR=10.11 dB. Top right: image restored by **BM3D**, PSNR=20.93 dB. Bottom left: image restored by **upBM3D**, PSNR=20.82 dB. Bottom right: image restored by **hybrid**, PSNR=20.85 dB. Right panel: Top: SSIM map for **BM3D**, SSIM=0.2459. Center: SSIM map for **upBM3D**, SSIM=0.3223. Bottom: SSIM map for **hybrid**, SSIM=0.3361

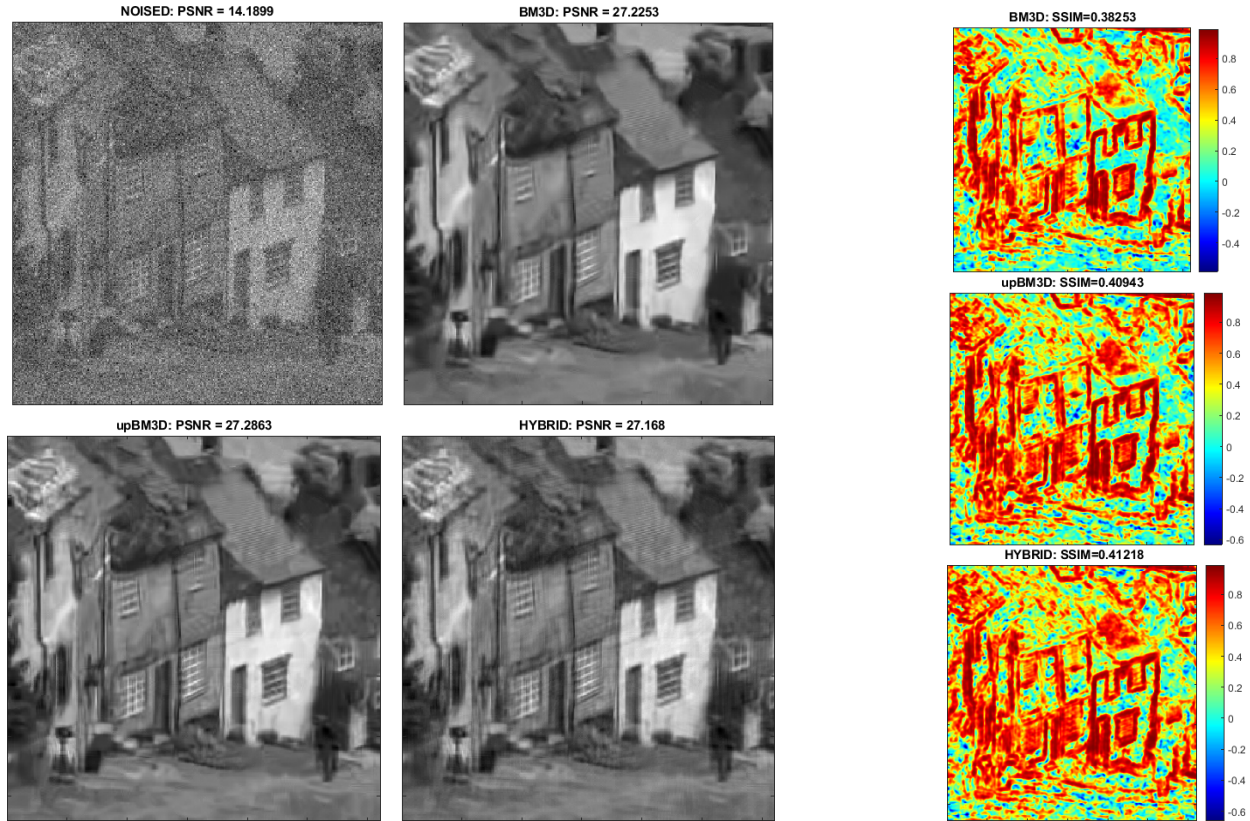


Figure 4.8: Restoration of "Goldhill" image corrupted by Gaussian noise with STD $\sigma = 50$ dB. Left panel: Top left: fragment of corrupted image, PSNR=14.19 dB. Top right: fragment of image restored by **BM3D**, PSNR=27.23 dB. Bottom left: fragment of image restored by **upBM3D**, PSNR=27.29 dB. Bottom right: fragment of image restored by **hybrid**, PSNR=27.17 dB. Right panel: Top: fragment of SSIM map for **BM3D**, SSIM=0.3825. Center: fragment of SSIM map for **upBM3D**, SSIM=0.4094. Bottom: fragment of SSIM map for **hybrid**, SSIM=0.4122

the combined algorithms. The combined algorithm runs fast. In most cases, it is sufficient to conduct two to three iterations (very rarely five to six iterations) in order to get an excellent result. For example, the Matlab implementation of three-iterations scheme takes about 15 seconds. where 11 seconds are consumed by the BM3D (MEX-files) and 3 seconds are consumed by a non-compiled version of the qWP denoising algorithm.

It is worth noting that our combined methods have some distant relation to the SOS boosting scheme presented in [14]. The main distinction between the qWPDn-BM3D and the SOS boosting is that each of the qWPDn and BM3D algorithms is “boosted” by the output from the other algorithm. Such a scheme can be regarded as a *CrossBoosting*.

Summarizing, having such a versatile and flexible tool as the directional qWPs that produce good results for denoising we are in a position to address data processing problems such as image inpainting, deblurring, superresolution, segmentation and classification, target detection (here the directionality is of utmost importance). Another potential application to be addressed is the extraction of characteristic features (feature selection) in multidimensional data in the deep learning framework. The 3D directional wavelet packets, whose design is underway, may be beneficial for seismic and hyper-spectral processing.

Acknowledgment This research was partially supported by the Israel Science Foundation (ISF, 1556/17), Blavatnik Computer Science Research Fund Israel Ministry of Science and Technology 3-13601 and 3-14481.

References

- [1] A. Averbuch, P. Neittaanmäki, and V. Zheludev. Analytic and directional wavelet packets in the space of periodic signals. arXiv:1907.01479 [math.NA].
- [2] A. Averbuch, P. Neittaanmäki, and V. Zheludev. *Splines and spline wavelet methods with application to signal and image processing, Volume III: Selected topics*. Springer, 2019.
- [3] Z. Che and X. Zhuang. Digital affine shear filter banks with 2-layer structure and their applications in image processing. *IEEE Trans. on Image Processing*, 27(8):3931–3941, 2018.
- [4] R. R. Coifman and V. M. Wickerhauser. Entropy-based algorithms for best basis selection. *IEEE Trans. Inform. Theory*, 38(2):713–718, 1992.
- [5] L. Şendur and I. W. Selesnick. Bivariate shrinkage functions for wavelet-based denoising exploiting interscale dependency. *IEEE Trans. Signal Process.*, 50:2744–2756, 2002.
- [6] K. Dabov, A. Foi, V. Katkovnik, and K. Egiazarian. Image denoising by sparse 3d transform-domain collaborative filtering. *IEEE Trans. Image Process.*, 16(8):2080–2095, 2007.
- [7] B. Goyal, A. Dogra, S. Agrawal, B.S. Sohi, and A. Sharma. Image denoising review: From classical to state-of-the-art approaches. *Information Fusion*, 55:220–244, 2020.
- [8] B. Han and Z. Zhao. Tensor product complex tight framelets with increasing directionality. *SIAM J. Imaging Sci.*, 7(2):997–1034, 2014.

- [9] B. Han, Z. Zhao, and X. Zhuang. Directional tensor product complex tight framelets with low redundancy. *Appl. Comput. Harmon. Anal.*, 41(2):603–637, 2016.
- [10] B. Han and X. Zhuang. Smooth affine shear tight frames with *MRA* structures. *Appl. Comput. Harmon. Anal.*, 39(2):300–338, 2015.
- [11] N.G. Kingsbury. Image processing with complex wavelets. *Philos. Trans. R. Soc. London A, Math. Phys. Sci.*, 357(1760):2543–2560, 1999.
- [12] N.G. Kingsbury. Complex wavelets for shift invariant analysis and filtering of signals. *J. Appl. Comput. Harm. Anal.*, 10(3):234–253, 2001.
- [13] A. V. Oppenheim and R. W. Schaffer. *Discrete-time signal processing*. Prentice Hall, New York, 3rd edition, 2010.
- [14] Y. Romano and M. Elad. Boosting of image denoising algorithms. *SIAM J. IMAGING SCIENCES*, 8(2):1187–1219, 2015.
- [15] L. Şendur and I. Selesnick. Bivariate shrinkage with local variance estimation. *IEEE Signal Process. Letters*, 9(12):438–441, 2002.
- [16] Zhou Wang, A. C. Bovik, H. R. Sheikh, and E. P. Simoncelli. Image quality assessment: from error visibility to structural similarity. *IEEE Trans. Image Process.*, 13(4):600–612, 2004.
- [17] H. Zhuang and B. Han. Compactly supported tensor product complex tight framelets with directionality. In *2019 International Conference on Sampling Theory and Applications (SampTA), Bordeaux, France*.
- [18] X. Zhuang. Digital affine shear transforms: fast realization and applications in image/video processing. *SIAM J. Imag. Sci.*, 9(3):1437–1466, 2016.